Multi-scale modelling of evolving plastic anisotropy during Al-alloy sheet forming

Wencheng Liu [a], Jia Huang [a], Yong Pang [c], Ke Zhu [d], Shugen Li [e], Jun Ma [b],*

[a] School of Civil Aviation, Northwestern Polytechnical University, Xi'an 710072, China
[b] Department of Mechanical and Industrial Engineering, Norwegian University of Science and Technology, Trondheim 7491, Norway
[c] Composites Research Group, University of Nottingham, Nottingham NG7 2RD, United Kingdom
[d] COMAC Flight Test Center, Shanghai 201323, China
[e] School of Mechanical Engineering, University of Shanghai for Science and Technology, Shanghai 200093, China

ARTICLE INFO

ABSTRACT

Accurate modelling of local evolving texture and yield surface evolution in complex strain path are of crucial importance to the accurate sheet metal forming simulations. This work proposed a novel multi-scale computational scheme, in which the full-field crystal plasticity (CP) modelling is mapped and real-time updated into each integration point following the local strain path in the finite element (FE) model. By the real-time close-loop feedback and update between the FE model and CP model, the evolving texture and its induced anisotropic plasticity evolution are considered utilizing on-the-fly virtual tests in the full deformation field. To carefully verify the developed computational framework, a comprehensive validation including plastic anisotropy characterization, cyclic hardening tests and deep drawing tests is conducted in an AA6016-T4 aluminium sheet with strong cube texture using ESAFORM Benchmark 2021. By comparison with experimental results and the conventional approaches with constant yield surface for the forming case, the newly developed method is thoroughly validated, showing that the significant texture evolution is observed in large plastic deformation and various strain paths lead to different texture evolution. The local evolving texture induced plastic anisotropy evolution has a considerable effect on the prediction accuracy of the deep drawing simulations, such as earing profile, wall thickness and loading history. Additionally, this method does not increase too much computation cost, enabling cost-effectively simulation of complex forming processes.

1. Introduction

Aluminium alloys have attracted increased applications in various areas, as their overall properties make them to be favoured for reducing the carbon footprint. Particularly, advanced aluminium alloy sheets are the preferred raw materials for manufacturing the auto body panel and other crucial thin-walled auto body structures in the automotive industry [1,2]. Aluminium sheets are normally fabricated through many complicated manufacturing processes including casting, homogenized, hot rolling, cold rolling, ageing, etc. The inhomogeneity of microstructure is introduced from this thermomechanical history, such as texture and inhomogeneous grain morphology. The strong texture would induce commonly observed mechanical anisotropy in such kinds of materials. The anisotropic property is normally undesired in the sheet metal forming industry, because it will result in significant problems affecting both dimensional accuracy and mechanical properties of formed components, such as localized distribution of thickness, earing,

crack, wrinkling and residual stress [3–6]. In addition, the evolving texture induced anisotropy evolution in large plastic deformation and Bauschinger behaviour in cyclic deformation are also widely observed in aluminium alloys [7,8], which makes the deformation behaviour more complex in actual forming processes. Therefore, to accurately predict the mechanical response and plastic deformation of the sheet metal in forming simulations, the development of suitable physical or virtual tests and constitutive models for evolving texture, plastic anisotropy evolution as well as Bauschinger behaviour are of crucial importance.

Experimentally, the mechanical anisotropy in different deformation paths can be obtained using various physical tests. Fig. 1 shows some well-established in-plane experimental method and their corresponding stress state. However, some of them require special equipment and can hardly be performed using a universal tensile machine. For example, the cruciform specimen in equibiaxial stress state requires a special
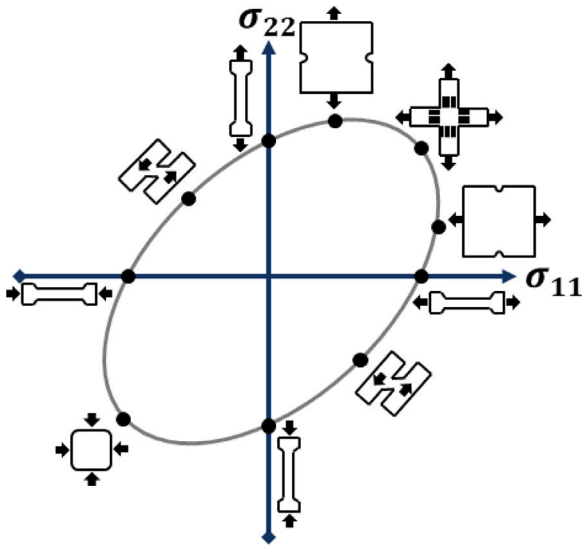
Fig. 1. Schematics of some well-known physical tests for the characterization of in-plane yield surface of the thin-walled specimens in the biaxial stress state, such as uniaxial tensile and compression tests, equibiaxial tensile tests, plane-strain tensile tests, pure shear tests and equibiaxial compression tests.

biaxial tensile machine and complex loading control method to ensure constant stress path [9,10]. Moreover, the twin bridge in-plane torsion test specimen in pure shear stress state must be conducted using an approximate support fixture [11,12]. Regarding the characterization of the Bauschinger effect of sheet metals, it also needs special equipment and tooling as well as related control methods to achieve the in-plane compression deformation. For example, the cyclic tension–compression test with normal contact forces applied to avoid the buckling is widely used to test the Bauschinger behaviour; however, friction effect and limited compression strain level still affect the test capability [13,14]. Despite these advanced experimental methods having achieved the mechanical responses of sheet metal in some specific stress states, accurate characterization of the plastic behaviour in arbitrary deformation mode and Bauschinger behaviour still remains challenging issues and it is also very time-consuming and costly although some existing test methods can be done.

In the last two decades, various advanced phenomenological yield functions have been developed to capture these experimental yield stresses and plastic potentials in different stress states. Based upon the concept of a linear transformation, several advanced anisotropic yield functions were developed to increase the flexibility by involving the linear transformation matrix, in which the complex variation of plastic anisotropy of strong textured metals can be accurately described. For instance, the two linear transformations based yield function so-called Yld2004-18p was proposed by Barlat et al. [15], which is suited for textured aluminium sheet [16]. Aretz and Barlat proposed an advanced yield function named Yld2011-27p associated with three linear transformations to overcome the lack of 'flexibility' of Yld2004-18p in describing the plastic anisotropy of strong textured metals [17]. Besides linear transformations based yield functions, Banabic et al. proposed a flexible yield criterion so-called BBC2003 [18] by adding weight coefficients to the isotropic formulation proposed by Hershey [19]. Later, two yield functions BBC2005 [20] and BBC2008 [21] were developed to improve the flexibility further. Recently, a flexible yield criterion was developed by Raemy et al. based on a Fourier series of the angular coordinates [22]. Hu et al. proposed a polynomial-type yield function, in which the parameters are directly defined by experimental r-value and yield stress without numerical fitting processes [23]. These phenomenological yield functions use physical mechanical tests to define the shape of the yield surface and are very useful in numerical

simulations to optimize the sheet metal forming process. However, the main drawback of this approach is that the evolution of yield surface shape cannot be captured during the plastic deformation. To overcome this limitation, a discrete framework was developed to describe the evolution of anisotropy by using various parameters of the yield function at discrete levels of plastic strain. For example, Safaei et al. proposed a phenomenological approach to describe the evolution of anisotropy in the uniaxial deformation path using sets of parameters associated with various equivalent plastic strain levels [24]. Yoshida et al. proposed an anisotropic yield function to describe the evolution of anisotropy and the Bauschinger effect, which is defined as an interpolation between two yield functions at two discrete levels of plastic strain [25]. Although the evolution of anisotropy in a specific strain path is successfully captured by this approach, the deformation behaviour in an arbitrary deformation path is still not accurately predicted.

Essentially, mechanical anisotropy is attributed to the distribution of orientations of crystalline aggregates, since mechanical anisotropy is inherent for a single crystal. For crystalline matter, various crystal plasticity (CP) approaches have been successfully developed and used to predict the plastic behaviour of crystalline aggregates at mesoscopic and engineering length scales. The CP approach could be briefly categorized as mean-field and full-field methods. For the mean-field CP method, Taylor proposed a full-constraint (FC) CP model using the iso-strain theory which leads to the violation of stress equilibrium [26]. Subsequently, extensive Taylor-type models were further developed to improve the condition of the stress equilibrium [27,28]. Due to this problem, the Taylor-type model cannot realistically describe the stress distribution among differently oriented grains during plastic deformation. To overcome the drawback of the Taylor-type model, various self-consistent (SC) models have been developed to describe the mechanical behaviour of polycrystals in various deformation modes [29–33]. Although the SC models simultaneously satisfy the stress equilibrium and the deformation compatibility, the main shortage of the mean-field method is still existing, i.e., the effect of some microstructural information is not accessible to SC models, such as the local latent hardening behaviour at the interface between the different grains and inhomogeneity of the intra-grain micro-mechanical field values [34]. Last decade, this microstructural information has been incorporated into the constitutive model using a full-field CP approach, where every single grain is discretized as a set of material points [35–38]. Full-field CP simulations can be used to predict the spatial distribution of both grain-to-grain interactions and intra-grain micromechanical field values [39–48]. Generally, full-field CP method utilizes the finite element method as the numerical solver, which is shorted as CPFEM [35]. Recently, the full-field CP modelling was successfully implemented in the fast Fourier transforms (FFTs) based spectral methods, which is shorted as CPFFT [49,50]. FEM approaches can be applied to predict the mechanical response of polycrystals under complex boundary conditions on arbitrary model geometries but they are very time-consuming [51]. Spectral methods are far more effective but only can solve the micro-mechanical field values of material points constrained by the periodic boundary conditions. When simulating the mechanical response of metallic materials at engineering-length scale, the homogenization schemes such as mean-field and grain-cluster homogenization within the numerical solution [35] are typically employed rather than the discrete structure with a large number of grains in full-field CP modelling. However, with respect to the prediction of plastic anisotropy evolution in large plastic deformation, full-field CP modelling is superior to these homogenization approaches [40, 52], but directly utilizing CP simulations in macro-scale structure, i.e., the initial blank is discretized as crystalline aggregates with a large number of material points, is not an ideal choice due to its very high computational cost [53]. To overcome the high computational cost of full-field CP modelling in solving micromechanical field values of a large number of grains at an engineering-length scale, the CP model is only employed to predict the initial plastic anisotropy data

required by the calibration of phenomenological yield function which is used to perform FE simulations at engineering-length scale [39–41,44,54,55]. These hierarchical schemes show several merits such as high computational efficiency, saving physical test costs and accurate prediction of anisotropic plasticity in arbitrary stress states. However, in these hierarchical schemes, the CP modelling is only performed once to calibrate the initial yield surface without the consideration of texture evolution induced yield surface change in complicated plastic strain path.

Additionally, the reverse loading and cyclic loading paths commonly occur during the sheet metal forming processes. It is known that the Bauschinger effect induced strength changes during the cyclic loading is more complex compared with the simple uniaxial tension. This behaviour can affect the quality of the formed part with respect to springback, residual stresses and thickness variation. Essentially, the Bauschinger behaviour is attributed to the residual stress in the grain boundary and texture evolution during the cyclic deformation [56]. In addition, the cyclic hardening behaviour of the precipitation-hardened aluminium alloys is influenced by the precipitation effect [57–59]. To capture this hardening response, many kinematic hardening models have been established by controlling the nonlinear motion and expansion of one-surface or multiple-surface [60–67], and trying to improve the FE simulation accuracy of sheet metal forming processes. These types of models have successfully reproduced the hardening curves in cyclic loading processes of various sheet metals in comparison with experimental results. However, physical testing of reverse loading-induced Bauschinger behaviour of thin-walled specimens at a large strain is still challenging, which makes some parameters of complicated kinematic hardening models hard to be obtained through physical tests. Since the grain boundary interaction and grain orientation rotation are taken into account in the full-field CP constitutive model, the Bauschinger behaviour of sheet metal can be predicted by full-field CP modelling [58,68–70]. CP simulations could predict the Bauschinger behaviour during the cyclic deformation at grain-length scale and further capture these cyclic hardening data at engineering-length scale [71–73], thus providing a feasible approach to calibrate the above-mentioned phenomenological kinematic hardening models.

To make an effort to solve the research gap described above, this research aims to develop a multi-scale model to describe the evolving texture induced plastic anisotropy evolution and Bauschinger behaviour during the large plastic deformation in strongly textured aluminium sheets, hence providing an accurate and high computation-efficiency approach for material modelling and simulation of forming processes. For this purpose, a novel microstructure-based computational framework is presented, where the high-efficiency spectral method based full-field CP modelling is embedded in the iterative process of FE simulations via user-material subroutine. In this scheme, each element has independent yield function coefficients and texture data which are updated by the full-field CP modelling following the strain path of the element, and hence, overcomes the main drawback of the current physical or virtual tests calibrated phenomenological yield functions, in which the shape of the yield surface is assumed as constant and same as the initial yield behaviour during the large plastic deformation. To verify the proposed multi-scale modelling method, the predicted uniaxial and biaxial mechanical anisotropy were compared with corresponding physical tests, and further experimental local texture evolution, earning profiles, loading history and the wall thickness variations in the cylindrical deep drawing provided by the ESAFORM Benchmark 2021 [1], were used to validate the simulation accuracy in sheet metal forming analysis. In addition, the conventional phenomenological models with constant yield surface calibrated by the physical experiments and virtual tests were also used in the simulation for comparison. The multi-scale modelling method proposed in this paper is formulated in a general form, which enables it to be readily utilized for other applications of material modelling and simulation, such as quick evaluation of formability, inverse design of microstructure design, optimization and control of forming processes and machine tools.

2. Multi-scale modelling framework

In the proposed microstructure-based computational framework considered the evolving texture, the full-field CP modelling and phenomenological constitutive model regularly interact to update the texture and plastic anisotropy at grain-length scale and engineering length scale, respectively. In the following subsections, the constitutive formulations of the employed full-field CP modelling, phenomenological yield functions and two-surface kinematic hardening model are briefly introduced to explain the meaning of the material constants. Their interactive algorithm in terms of real-time close-loop feedback and updates is introduced in detail.

2.1. Finite strain crystal plasticity theory

In the finite strain CP theory, the deformation gradient was utilized to describe the stretch, rotation and shear of the crystal lattice in the deformation field. Mathematically, the deformation gradient can be decomposed as two components, i.e, elastic and plastic $\mathbf{F} = \mathbf{F}_e \mathbf{F}_p$. The evolution of deformation gradients are governed by velocity gradients $\mathbf{L}_e$ and $\mathbf{L}_p$ using the following flow rule $\mathbf{L} = \mathbf{L}_e + \mathbf{F}_e \mathbf{L}_p (\mathbf{F}_e)^{-1}$, where the plastic velocity gradient $\mathbf{L}_p$ due to dislocation slip is expressed as the sum over the individual shear contribution $\dot{\gamma}^\alpha$ on the number of N slip systems α:

$$\mathbf{L}_p = \dot{\mathbf{F}}_p \mathbf{F}_p^{-1} = \sum_\alpha^N \dot{\gamma}^\alpha \mathbf{s}_0^\alpha \otimes \mathbf{m}_0^\alpha \tag{1}$$

where the $\mathbf{s}_0^\alpha$ and $\mathbf{m}_0^\alpha$ are unit vectors which determine the shear deformation mode and the direction of its deformation plane normal to the slip systems in the deformation field through the dyadic product of the Schmid components. The well-known power law [74,75] was applied to describe the plastic shear rate $\dot{\gamma}^\alpha$:

$$\dot{\gamma}^\alpha = \dot{\gamma}^0 \left| \frac{\tau_a}{g^\alpha} \right|^{1/m} sgn(\tau_a) \tag{2}$$

where the deformation rate $\dot{\gamma}^0$ and exponent m respectively define the reference and strain rate sensitivity of the crystalline deformation. The slip resistance g^α determines the micro-mechanical strain hardening response of the material points in the current deformation field, which progressively evolves from g_0 to g_∞ [76]. The constitutive formulation for describing the evolution of g^α during the plastic deformation is determined by its rate:

$$\dot{g}^\alpha = \sum_\beta^N h_{\alpha\beta} \dot{\gamma}^\beta \tag{3}$$

where $g^\alpha(0) = g_0$ defines the initial slip resistance stress for the specific slip deformation mode of each material point, and the strain hardening matrix $h_{\alpha\beta}$ determines the instantaneous slip resistance stress in the current deformation field which is formulated by:

$$h_{\alpha\beta} = h_0 \left[q + (1-q)\delta_{\alpha\beta} \right] \left| 1 - \frac{g^\beta}{g_\infty} \right|^a sgn\left(1 - \frac{g^\beta}{g_\infty}\right) \tag{4}$$

where q is a latent hardening parameter which is taken by 1 to 1.4 for various slip systems to describe the different latent hardening levels. Moreover, the strain hardening of the material points is also governed by the other material constant h_0, a and saturated slip resistance stress g_∞, which are obtained by optimized numerical fitting processes.

To obtain the stress state of the crystal, the applied shear stress τ^α is needed to be transformed to the Cauchy stress component σ through the numerical solved second Piola–Kirchhoff stress component $\mathbf{S}$ [35]:

$$\tau^\alpha = \sigma : \left(\mathbf{F}_e \mathbf{S}_0^\alpha \mathbf{F}_e^{-1}\right) = \left(\mathbf{F}_e^T \mathbf{F}_e \mathbf{S}\right) : \mathbf{S}_0^\alpha \tag{5}$$

where the second Piola–Kirchhoff stress $\mathbf{S}$ can be numerically solved utilizing the finite elastic strain theory:

$$\mathbf{S} = \mathbb{C} : \mathbf{E}_e \quad \text{with} \quad \mathbf{E}_e = \left(\mathbf{F}_e^T \mathbf{F}_e - \mathbf{I}\right)/2 \tag{6}$$

where $\mathbb{C}$ is the elastic stiffness matrix which determines the stress–strain behaviour of crystal in elastic deformation. For cubic crystals, $\mathbb{C}$ is symmetrically formulated by three elastic constants C_{11}, C_{12}, and C_{44}.

The full-field CP model has been implemented into an open-source spectral method solver DAMASK [42], and the elaborated implementation method of the finite strain CP constitutive model into the spectral numerical solver could be founded in the Ref. [50]. The crystal plasticity modelling was used to virtually test material response under various loading scenarios for characterizing the plastic anisotropy and the Bauschinger effect, thus providing the required data for calibrating the phenomenological models.

2.2. Formulations of phenomenological model

The phenomenological yield functions are popularly utilized to predict the mechanical response and plastic deformation of sheet metals due to their user-friendly formulations and easy implementation in the user material subroutine of FE numerical solver. Two phenomenological yield functions, i.e., Yld2000-2d and Yld2004-18p subjected to in-plane and 3D stress states, respectively, [15,77], are utilized in this research to model the anisotropy of strongly textured aluminium alloys. The implementation of the Yld2000-2d into FE simulations has gained considerable popularity for forming simulations of various sheet metals. This yield function is based on linear transformations of two unconditionally convex functions φ' and φ'' of the deviatoric stress tensor.

$$f(\sigma) = \left[\frac{1}{2}(\varphi' + \varphi'')\right]^{1/a} = \bar{\sigma} \tag{7}$$

where

$$\varphi' = (X'_1 - X'_2)^a, \varphi'' = (2X''_2 + X''_1)^a + (2X''_1 + X''_2)^a \tag{8}$$

where the exponent a determines the ellipsoid of the yield surface, which is generally taken by 6 and 8 for steel and aluminium alloy, respectively. The $\bar{\sigma}$ is the effective stress. The X' and X'' are the principal values of linear transformed stress matrices, which are calculated by the multiplier of the linear transformation matrix and in-plane CAUCHY stress tensor, $\sigma = [\sigma_{11} \ \sigma_{22} \ \sigma_{12}]^T$:

$$\tilde{x}' = L' : \sigma \tag{9}$$

$$\tilde{x}'' = L'' : \sigma \tag{10}$$

where the linear transformations were defined as:

$$\begin{bmatrix} L'_{11} \\ L'_{12} \\ L'_{21} \\ L'_{22} \\ L'_{66} \end{bmatrix} = \begin{bmatrix} 2/3 & 0 & 0 \\ -1/3 & 0 & 0 \\ 0 & -1/3 & 0 \\ 0 & 2/3 & 0 \\ 0 & 0 & 1 \end{bmatrix} \begin{bmatrix} a_1 \\ a_2 \\ a_7 \end{bmatrix}, \tag{11}$$

$$\begin{bmatrix} L'_{11} \\ L'_{12} \\ L'_{21} \\ L'_{22} \\ L'_{66} \end{bmatrix} = \frac{1}{9} \begin{bmatrix} 2 & -2 & 8 & -2 & 0 \\ 1 & -4 & -4 & 4 & 0 \\ 4 & -4 & -4 & 1 & 0 \\ -2 & 8 & 2 & -2 & 0 \\ 0 & 0 & 0 & 0 & 9 \end{bmatrix} \begin{bmatrix} a_3 \\ a_4 \\ a_5 \\ a_6 \\ a_8 \end{bmatrix} \tag{12}$$

Based on the good flexibility of the Yld2000-2d, the in-plane mechanical anisotropy could be appropriately described in this yield function. However, the out-of-plane anisotropy cannot be considered in this model. Therefore, the Yld2004-18p yield function considered 3D stress tensor is also utilized to calibrate both in-plane and out-of-plane plastic anisotropy of the materials. This yield function has been found to have good high accuracy in describing the plastic anisotropy of textured aluminium alloys in full-stress space. The formulation of this phenomenological 3D yield criterion is expressed as [15]:

$$\Psi\left(\tilde{S}', \tilde{S}''\right) = \left|\tilde{S}'_1 - \tilde{S}''_1\right| + \left|\tilde{S}'_1 - \tilde{S}''_2\right| + \left|\tilde{S}'_1 - \tilde{S}''_3\right| + \left|\tilde{S}'_2 - \tilde{S}''_1\right|$$
$$+ \left|\tilde{S}'_2 - \tilde{S}''_2\right| + \left|\tilde{S}'_2 - \tilde{S}''_3\right| + \left|\tilde{S}'_3 - \tilde{S}''_1\right| \tag{13}$$
$$+ \left|\tilde{S}'_3 - \tilde{S}''_2\right| + \left|\tilde{S}'_3 - \tilde{S}''_3\right| = 4\bar{\sigma}^a$$

where $\bar{\sigma}$ is the effective stress and the exponent a determines the ellipsoid of the yield surface. The $\tilde{S}'_i$ and $\tilde{S}''_i$ ($i = 1,2,3$) are the principal values of the linear transformed stress matrices $\tilde{s}'$ and $\tilde{s}''$ which can be obtained by employing linear transformations on Cauchy stress deviators.

$$\tilde{s}' = C' : T : \sigma, \quad \tilde{s}'' = C'' : T : \sigma \tag{14}$$

$$\sigma = \begin{bmatrix} \sigma_{xx} & \sigma_{yy} & \sigma_{zz} & \sigma_{xy} & \sigma_{yz} & \sigma_{zx} \end{bmatrix}^T \tag{15}$$

where C' and C'' are the linear transformations on the stress deviators and are given as follows:

$$C' = \begin{bmatrix} 0 & -\alpha_1 & -\alpha_2 & 0 & 0 & 0 \\ -\alpha_3 & 0 & -\alpha_4 & 0 & 0 & 0 \\ -\alpha_5 & -\alpha_6 & 0 & 0 & 0 & 0 \\ 0 & 0 & 0 & \alpha_9 & 0 & 0 \\ 0 & 0 & 0 & 0 & \alpha_7 & 0 \\ 0 & 0 & 0 & 0 & 0 & \alpha_8 \end{bmatrix}, \tag{16}$$

$$C'' = \begin{bmatrix} 0 & -\alpha_{10} & -\alpha_{11} & 0 & 0 & 0 \\ -\alpha_{12} & 0 & -\alpha_{13} & 0 & 0 & 0 \\ -\alpha_{14} & -\alpha_{15} & 0 & 0 & 0 & 0 \\ 0 & 0 & 0 & \alpha_{18} & 0 & 0 \\ 0 & 0 & 0 & 0 & \alpha_{16} & 0 \\ 0 & 0 & 0 & 0 & 0 & \alpha_{17} \end{bmatrix} \tag{17}$$

T is the constant linear transformation described as:

$$T = \frac{1}{3} \begin{bmatrix} 2 & -1 & -1 & 0 & 0 & 0 \\ -1 & 2 & -1 & 0 & 0 & 0 \\ -1 & -1 & 2 & 0 & 0 & 0 \\ 0 & 0 & 0 & 3 & 0 & 0 \\ 0 & 0 & 0 & 0 & 3 & 0 \\ 0 & 0 & 0 & 0 & 0 & 3 \end{bmatrix} \tag{18}$$

The anisotropy parameters α_i of the linear operators C' and C'' determine the plastic anisotropy and shape of the yield surface by adding the weight coefficients on the stress components. In the conventional method, the in-plane parameters are normally determined by using the directional r-values, stresses in uniaxial and biaxial tension, and plastic potentials. However, four parameters of the linear transformations, namely $\alpha_7^{(k)}$, $\alpha_8^{(k)}$, $\alpha_{16}^{(k)}$ and $\alpha_{17}^{(k)}$ are determined by the out-of-plane mechanical anisotropy, which is difficult to be measured experimentally for thin-walled sheets. The CP simulations could be utilized to predict the yield stress and plastic strain in arbitrary deformation mode, and hence these out-of-plane parameters could be calibrated.

In this work, two sets of coefficients of Yld2000-2d and Yld2004-18p models were established based on full-field CP simulations and physical experiments, respectively. The Yld2000-2d and YLD2004-18p models were implemented into ABAQUS implicit solver via user-material subroutine using a fully implicit back-Euler stress integration approach.

2.3. Two-surface kinematic hardening model

Conventionally, the implementation of yield function into FE code is associated with phenomenological isotropic hardening model such as Swift and Voce hardening laws. However, in many practical sheet forming processes, the material would suffer a complex strain history, in which reverse loading and cyclic deformation commonly occur. Under cyclic deformation and reverse loading path, the material usually can present kinematic hardening behaviour, which cannot be described by the isotropic hardening model. To capture this hardening phenomenon, a two-surface model was proposed by Yoshida and Uemori [60,64,78]. This hardening model is consist of a yield surface and a bounding surface, in which the kinematic hardening behaviour is described by moving the yield surface within the bounding surface. The experimental results approved that this two-surface model could capture the kinematic hardening behaviours using a small number of parameters. In this research, an associated flow rule based two-surface hardening model is proposed in this work, which is modified from the non-associated flow rule based two-surface model proposed by the Ghaei et al. [65]. This hardening model was incorporated with the advanced yield function to describe the complex deformation behaviour in sheet metal forming. In this model, the yield criterion f_y determines the boundary between the elastic and plastic zone using yield stress y in the

stress space and the function F determines the shape of the bounding surface, as given by:

$$f_y(\eta) - y = 0 \tag{19}$$

$$F(\Sigma - \alpha_2) - b_0 - r(p) = 0 \tag{20}$$

$$\eta = \sigma - \alpha \tag{21}$$

where σ is the Cauchy stress tensor in the current state and the backstress tensor α controls the movement of the yield surface. η is substituted into the yield criterion to calculate the effective stress. Σ is the corresponding stress point on the bounding surface, α_2 is the corresponding backstress tensor and b_0 is the initial size of bounding surface. r controls the expansion of the bounding surface, which is governed by the equivalent plastic strain p:

$$r(p) = Q\left[1 - \exp(-bp)\right] \tag{22}$$

where the Q and b are the material constants that need to be calibrated. In this model, the kinematic hardening behaviour is governed by the state of the backstress $\dot{\alpha}$, which can be decomposed as $\dot{\alpha} = \dot{\alpha}_1 + \dot{\alpha}_2$. The $\dot{\alpha}_1$ is dependent on the rate of equivalent plastic strain $\dot{p}$, and can be described by:

$$\dot{\alpha}_1 = \gamma_1 \left(\frac{b_0 + r - y}{y} \eta - \alpha_1 \right) \dot{p} \tag{23}$$

where γ_1 is the material constant and b_0 determines the initial size of the bounding surface. α_1 is the deviation between the central position of the yield surface and the bounding surface. The motion of the bounding surface is controlled through the $\dot{\alpha}_2$, as given by:

$$\dot{\alpha}_2 = \gamma_2 \left(\frac{c_2}{y} \eta - \alpha_2 \right) \dot{p} \tag{24}$$

where c_2 and γ_2 are the material parameters. α_2 is the central position of the bounding surface in the stress space. To obtain the equivalent plastic strain rate $\dot{p}$, the classical associated flow rule (AFR) is employed by:

$$\dot{\varepsilon}^p = \dot{\lambda} \frac{\partial f_y}{\partial \sigma} = \dot{\lambda} m \tag{25}$$

where $\dot{\varepsilon}^p$ is the rate of the plastic strain tensor and $\dot{\lambda}$ is the plastic multiplier, which is same as the equivalent plastic strain rate in AFR, i.e., $\dot{p} = \dot{\lambda}$. m is the first order of the yield function, which makes the plastic potentials normal to the yield surface. A consistency condition in the yield surface and bounding surface is utilized to solve the equivalent plastic strain rate:

$$\frac{\partial f_y}{\partial \sigma} : \dot{\sigma} + \frac{\partial f_y}{\partial \alpha_1} : \dot{\alpha}_1 + \frac{\partial f_y}{\partial \alpha_2} : \dot{\alpha}_2 = m : \dot{\eta} = 0 \tag{26}$$

Here, the elastic stress tensor follows Hooke's law, and hence the rate of the stress tensor is obtained by:

$$\dot{\sigma} = D : (\dot{\varepsilon} - \dot{\varepsilon}^p) = D : (\dot{\varepsilon} - \dot{\lambda} m) \tag{27}$$

where D is the elastic stiffness matrix, and $\dot{\varepsilon}$ is the rate of total strain tensor. The plastic multiplier can thus be represented by substituting Eq. (27) into Eq. (26), as given by:

$$m : D : (\dot{\varepsilon} - \dot{\lambda} m) - m : \dot{\alpha}_1 - m : \dot{\alpha}_2 = 0 \tag{28}$$

Therefore, the plastic multiplier (equivalent plastic strain rate) can be obtained by substituting Eqs. (23) and (24) into Eq. (28) and using AFR $\dot{p} = \dot{\lambda}$, which is denoted by:

$$\dot{p} = \frac{m : D : \dot{\varepsilon}}{m : D : m + m : \frac{\dot{\alpha}_1}{\dot{p}} + m : \frac{\dot{\alpha}_2}{\dot{p}}} \tag{29}$$

In addition, by substituting Eq. (29) into Eq. (27), the tangent consistent modulus D^{ep} of the two-surface hardening model is determined:

$$\dot{\sigma} = D^{ep} : \dot{\varepsilon} = \left(D - \frac{(D : m) \otimes (D : m)}{m : D : m + m : \frac{\dot{\alpha}_1}{\dot{p}} + m : \frac{\dot{\alpha}_2}{\dot{p}}} \right) \tag{30}$$

Besides the permanent softening, the work hardening stagnation is another phenomenon that about zero strain hardening rate is observed at the early stage of reverse loading [60]. To describe this phenomenon, a stagnation surface is introduced to limit the expansion of the bounding surface. In this method, the expansion of the bounding surface is only allowed when the central position of the bounding surface is within the range of the stagnation surface. This stagnation surface is given as follows:

$$f_s(\alpha_2 - \alpha_s) - y_s = 0 \tag{31}$$

where y_s and α_s is the initial size and the central location of the stagnation surface in stress space. A non-linear kinematic hardening law is utilized to describe the translation of the bounding surface:

$$\dot{\alpha}_s = \dot{\mu}(\alpha_2 - \alpha_s) = \dot{\mu}\xi \tag{32}$$

where the tensor ξ and rate $\dot{\mu}$ are achieved using the following criterion:

$$\frac{\partial f_s}{\partial \alpha_2} : \dot{\alpha}_2 + \frac{\partial f_s}{\partial \alpha_s} : \dot{\alpha}_s - \dot{y}_s = 0 \tag{33}$$

where the $\dot{\mu}$ is obtained by substituting Eq. (32) into Eq. (33):

$$\dot{\mu} = \frac{n : \dot{\alpha}_2 - \dot{y}_s}{n : (\alpha_2 - \alpha_s)} \tag{34}$$

where $n = \frac{\partial f_s}{\partial \alpha_2}$. The rate of y_s is defined as:

$$\dot{y}_s = h n : \dot{\alpha}_2, \quad \text{when} \quad \dot{r} > 0 \tag{35}$$

$$\dot{y}_s = 0, \quad \text{when} \quad \dot{r} = 0 \tag{36}$$

where h is the experiment calibrated material constant, which controls the expansion level of the stagnation surface. The $\dot{r}$ determines that the stagnation surface is only allowed to expand associated with the expansion of the bounding surface.

2.4. Multi-scale modelling scheme for evolving texture and anisotropic plasticity

The two types of the constitutive models presented above are performed in different types of numerical solvers, where the DAMASK full-field crystal plasticity model is FFTs based spectral solver included in Portable, Extensible Toolkit for Scientific Computation (PETSc) and the phenomenological yield function and two-surface kinematic hardening model is implemented into the ABAQUS/UMAT subroutine. Therefore, they are difficult to be integrated into the same numerical scheme. In this work, the shell script in the Linux platform is used to achieve the "coupling" between DAMASK and ABAQUS through data transferring with updated texture information and coefficients of anisotropic plasticity models.

Fig. 2 indicates the schematic presentation of one computational loop in the multi-scale modelling involving texture and anisotropic plasticity evolution. In this process, the strain path of each integration point solved by finite element modelling is passed to the full-field CP modelling as the boundary condition. Thus, the strain path dependent texture updates are achieved utilizing the mapped RVEs in CP modelling. Subsequently, the virtual tests are conducted using the RVE with updated texture to calibrate the new parameters of the yield function, which are returned to the corresponding integration point in the macroscopic finite element model. The detailed computational processes are stated in the following. In the beginning, the UMAT subroutine loop is performed using the initial yield function coefficients which are identified by the full-field CP modelling using the initial
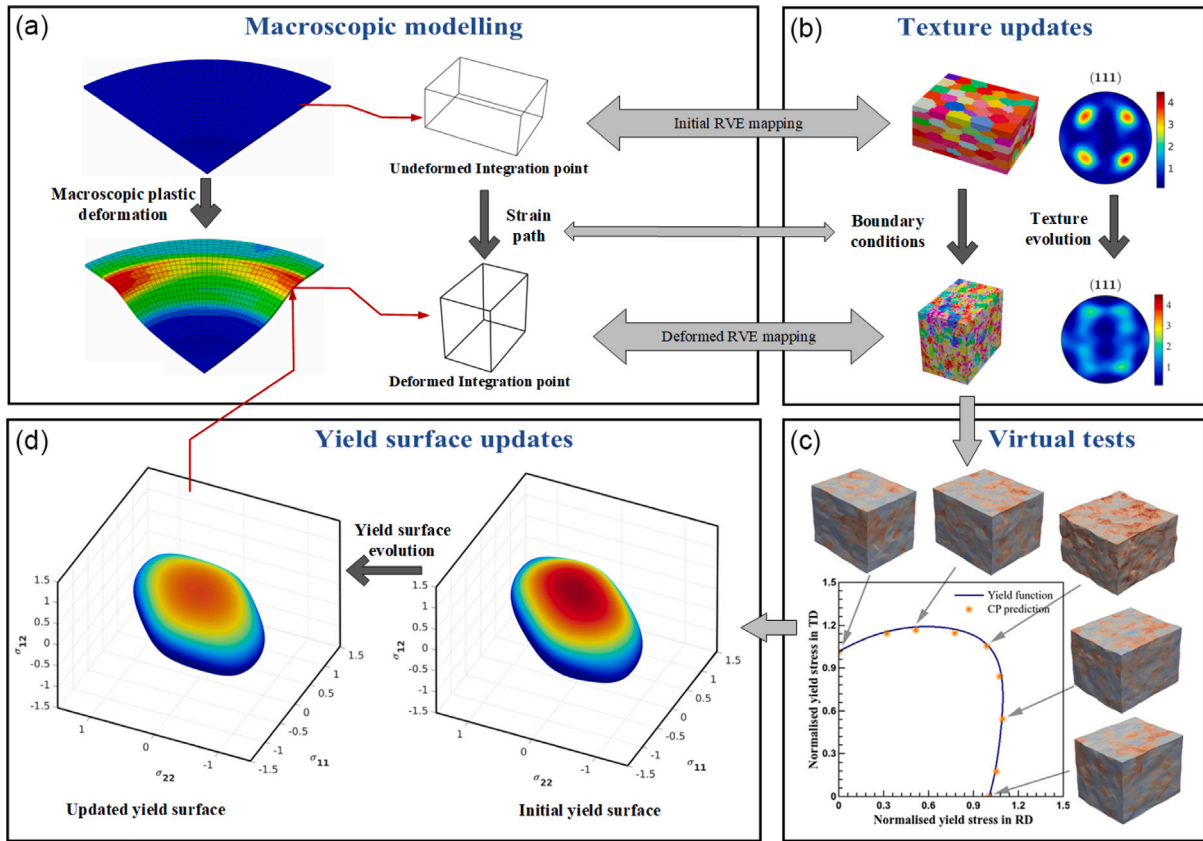
Fig. 2. Schematics of the one computational loop in the evolving texture based multi-scale modelling schemes including four steps: (a) Macroscopic finite element modelling and local strain path output, (b) full-field CP simulations based strain path dependent texture updates for each integration points, (c) New texture based virtual tests and (d) new yield surface calibration and updates.

texture of the material before forming. Meanwhile, the accumulated equivalent plastic strain and each strain tensor component are stored in the UMAT solution-dependent variables (SDV), denoted as SDV_{EQS} and $SDV_{\epsilon_{ij}}$. When the accumulated equivalent plastic strain exceeds a predefined threshold, the UMAT is paused and DAMASK full-field CP modelling is executed through the shell script. In the class of full-field CP modelling, the updated texture data is solved by the RVE in the periodical boundary conditions (BCs), which is consistent with the accumulated strain $SDV_{\epsilon_{ij}}$ of the element in UMAT (the detail see Appendix). Subsequently, the updated texture data are employed to perform several virtual mechanical tests, including directional tensile tests from RD to TD at an interval of 15° in the RD-TD plane, biaxial tensile tests in RD-TD, TD-ND and RD-ND planes. These mechanical anisotropy data obtained from CP virtual tests are then used to calibrate the new coefficients of the yield function at the current deformation state. Once the strain path dependent texture and yield function coefficients are updated, SDV_{EQS} and $SDV_{\epsilon_{ij}}$ reset as zero and the loop of UMAT continues working to update σ and SDVs using the updated yield functions until accumulated equivalent plastic strain reaches next threshold value. It should be noted that each element has its independent UMAT loop, where the local deformation history is passed to full-field CP modelling for updating the texture and yield function coefficients. Therefore, the yield surface evolution at each element depends on the local texture evolution induced by local plastic deformation history.

3. Material characterization and cup drawing experiments

The as-received material is an AA6016-T4 sheet with 1 mm thickness, supplied by the UACJ Co., Japan. In this Section, the crystalline morphology and texture of the as-received AA6016-T4 sheet are characterized by high-resolution EBSD tests, which are utilized to establish the accurate RVEs. The directional uniaxial, biaxial tests and shear tests are conducted to obtain the plastic anisotropy and provide validation data of virtual tests. Cylindrical cup drawing tests are performed to verify the accuracy of the evolving texture based model and conventional approach with a constant yield surface.

3.1. Microstructure characterization

High-resolution electron backscatter diffraction (EBSD) tests were performed at the University of Aveiro utilizing a Bruker CrystAlign QC 400 EBSD system interfaced to a Hitachi SU-70 SEM to examine the crystallographic texture of the as-received AA6016-T4 sheet, by the organizers of the ESAFORM Benchmark 2021. The source EBSD data can be found in [1] An open-source EBSD post-analysis software package MTEX was used to analyse the raw EBSD results [80]. As shown in Fig. 3a, it can be found from the inverse pole figure that most of the grain shapes of AA6016-T4 are equiaxial. Furthermore, the orientation density function (ODF) was analysed. Fig. 3b shows the corresponding sliced orientation density maps through the reduced Euler space $\left(0° \leq \{\phi_1, \Phi, \phi_2\} \leq 90°\right)$ in Bunge's convention. It can be observed that the highest ODF intensity is about 20, located in $\{\phi_1, \Phi, \phi_2\} = \{0°, 0°, 0°\}$. Based on the above analysis, a pronounced cube texture can be found in the AA6016-T4 sheet.

3D RVE crystal plasticity (CP) modelling was developed for the AA6016-T4 sheet, based on the measured microstructure features in above. The CP model will be used to predict the macro-scaled response of mechanical anisotropy for AA6016-T4. Since the accuracy of the full-field CP modelling in the prediction of macro-scaled anisotropy may be sensitive to the number of grains, five periodic cubic RVEs
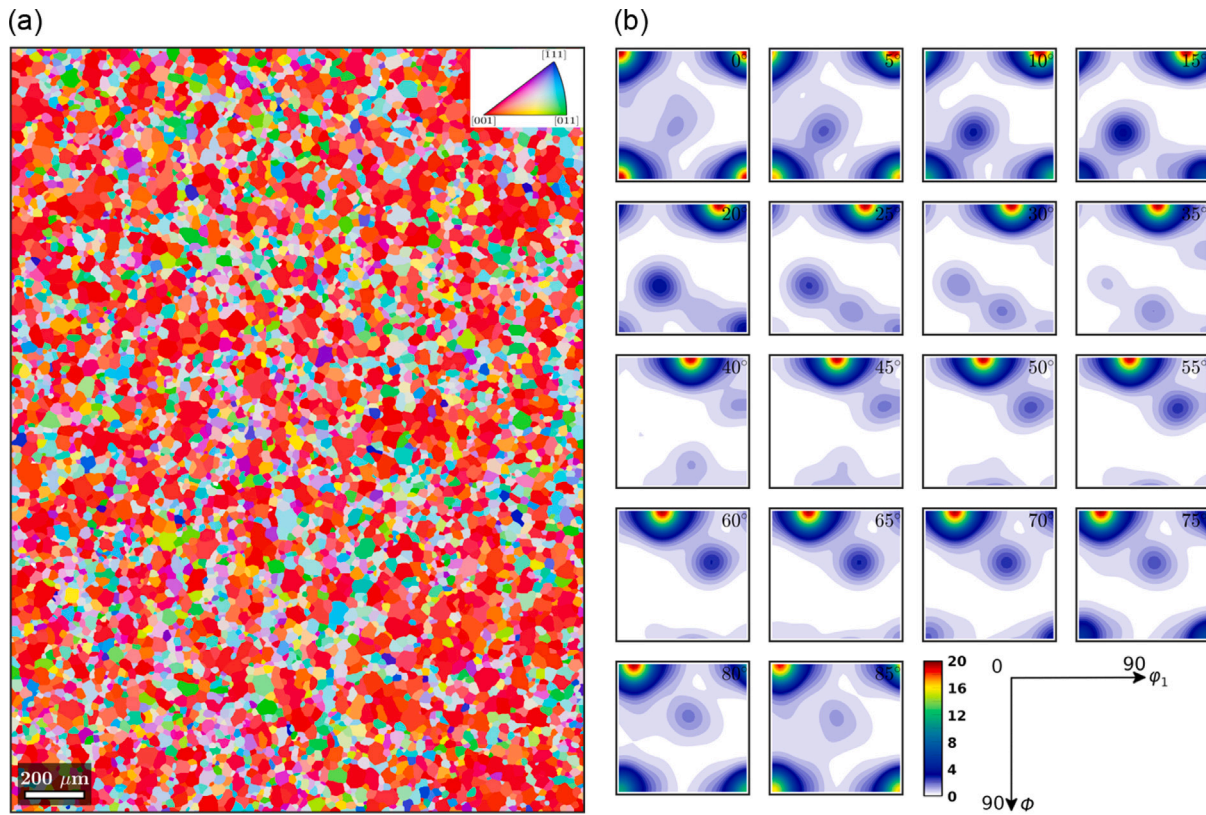
Fig. 3. Microstructure characterization of as-received AA6016-T4 aluminium alloy sheet. (a) 1.9 mm × 2.6 mm EBSD map with inverse pole figure colour, where the *x*-direction is RD (rolling direction) and *y*-direction is TD (transverse direction) [1]. (b) The orientation density map of orientation density function (ODF) as sections through the reduced Euler space for cubic-orthorhombic symmetry, where a strong cube texture is observed in the ODF.
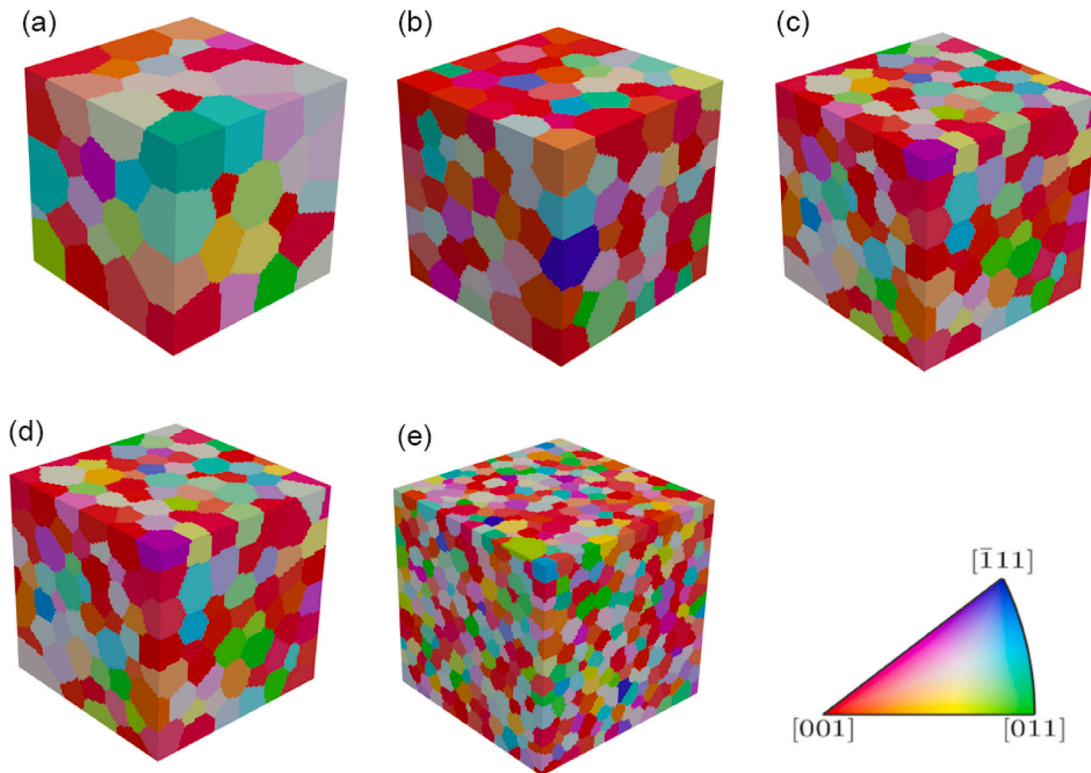

Fig. 4. The Voronoi tessellation generated 3D RVE with a resolution of 80 × 80 × 80 Fourier points using open-source software neper [79] for (a) 100, (b) 300, (c) 500, (d) 1000 and (e) 3000 equiaxial grains used for the grain number sensitivity study of virtual tests, and their orientations following the same EBSD data based ODF and are represented using inverse pole figure colourmap.

Table 1
The CP constitutive parameters for the AA6016-T4 aluminium alloy sheet, identified according to the experimental data of uniaxial tension and shear along RD.

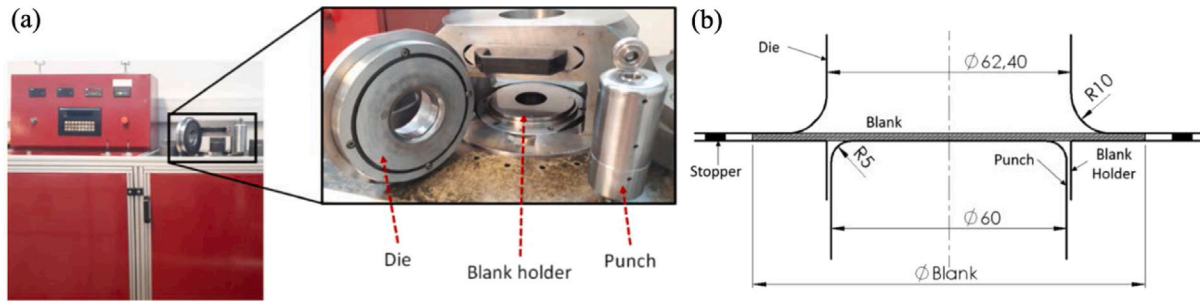| C_{11}	C_{12}	C_{44}	$\dot{\gamma}_0$	h_0	g_0	g_∞	m	a	q
82 GPa	62 GPa	29 GPa	0.001 s^{-1}	1140 MPa	48 MPa	140 MPa	0.02	2.0	1.4

Fig. 5. Experimental set-up for cup drawing tests [1]: (a) Schematics of the hydraulic universal testing machine and tooling parts (composed of four parts: a die, a blank holder, a cylindrical punch and a stopper) for cylindrical cup drawing experiments. (b) The geometry of the tooling system (dimension in mm) for cylindrical cup drawing experiments. The initial diameter of the blank is 107.50 mm and the blank holder force was set as 40 kN.

consisting of 100, 300, 500, 1000 and 3000 grains (Fig. 4) were employed in the convergence study (each grain was illustrated by its inverse pole figure colour). The crystalline morphology of these RVEs is set as equiaxial grain, which is obtained using the software Neper based upon the Voronoi tessellation method. The resolution of the RVE is defined as $80 \times 80 \times 80$ Fourier points (total of 512,000 voxels). Based on the results in Ref. [49], the predicted mechanical response is virtually converged for a spectral method based CP modelling when the resolution of RVEs exceeds $32 \times 32 \times 32$. Therefore, the resolution of $80 \times 80 \times 80$ could obtain converged results. The orientations of the grains in the five 3D RVEs were generated from the same ODF based on the 2D EBSD data in the RD-TD plane. Since the as-received AA6016-T4 sheet is treated by temper 4 (solution heat treatment and naturally aged), the strong cube texture and equiaxial grain shape are introduced by the recrystallization temperature in solution heat treatment. This temperature treatment has the same effect in the RD-TD plane and thickness direction. This assumption is supported by the EBSD data of the AA6016-T4 sheet in the RD-ND plane reported in Ref. [81], which shows the equiaxial grain morphology and the texture along the thickness direction also complies with the strong cube texture. Therefore, the texture of 3D RVEs obtained from the 2D EBSD data in the RD-TD plane appropriately represents the texture of the AA6016-T4 sheet.

3.2. Mechanical characterization

Uniaxial and biaxial tension tests were used to verify the accuracy of the CP virtual testing method developed above. These mechanical experiments for AA6016-T4 were conducted at the Tokyo University of Agriculture and Technology by the organizers of the ESAFORM Benchmark 2021 and can be found in [1]. The uniaxial tensile tests were performed from 0° to 90° at an interval of 15°. The strain rate was set as approximately 5×10^{-4}/s. It is noted that the biaxial tension tests under proportional loading with the seven stress ratios (4:1, 2:1, 4:3, 1:1, 3:4, 1:2, and 1:4) were conducted using cruciform specimens. More details about the biaxial tension tests using cruciform specimens can be found in Ref. [9,10]. In addition, shear and reverse shear tests were conducted by the organizers of the ESAFORM Benchmark 2021 [1], in which the deformation zone of the shear testing specimen is 30 mm × 3 mm, and the crosshead speed during shear deformation was set as 1 mm/min.
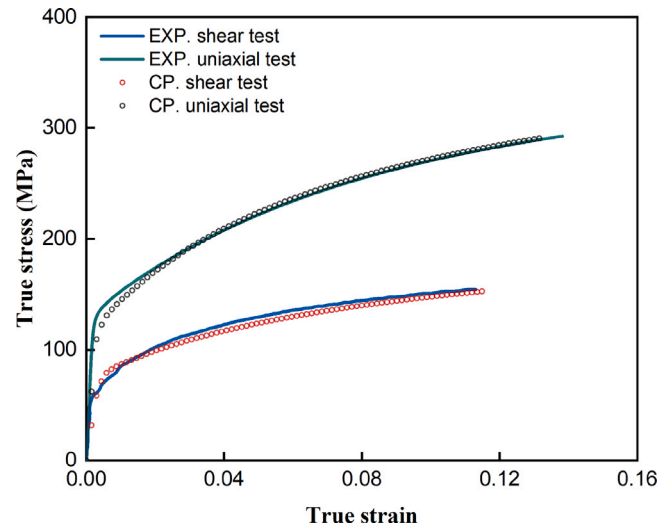

Fig. 6. True stress versus true strain curves of AA6016-T4 during the uniaxial tensile test and pure shear test predicted by CP model using the optimized solution of material constant (documented in Table 1), which leads to the computed stress–strain curve adjusted to experimental data after the iterative global optimization.

3.3. Cup drawing experiments and FE modelling

The cylindrical cup drawing experiments were used to validate the capability of developed constitutive models, with a focus on the analysis of earing profile, thickness variation and punch force. The forming experiments were conducted at the University of Porto by the organizers of the ESAFORM Benchmark 2021 and have been documented in [1]. These cup drawing experiments were carried out at a punch speed of 0.5 mm/s. The tooling system of cup drawing is illustrated in Fig. 5, including punch, blank holder, lower die and stopper. The initial diameter of the AA6016-T4 blank is 107.50 mm. A constant blank holder force of 40 kN was used during the cup drawing process.

In this study, a finite element model of the AA6016-T4 sheet cup drawing was established based on the ABAQUS platform. The tools described above in the forming process were modelled as rigid bodies. The AA6016-T4 sheet blank was meshed by shell element S4R and solid element C3D8R for Yld2000-2d and Yld2004-18p models, respectively. The Coulomb model was employed, with a constant coefficient of
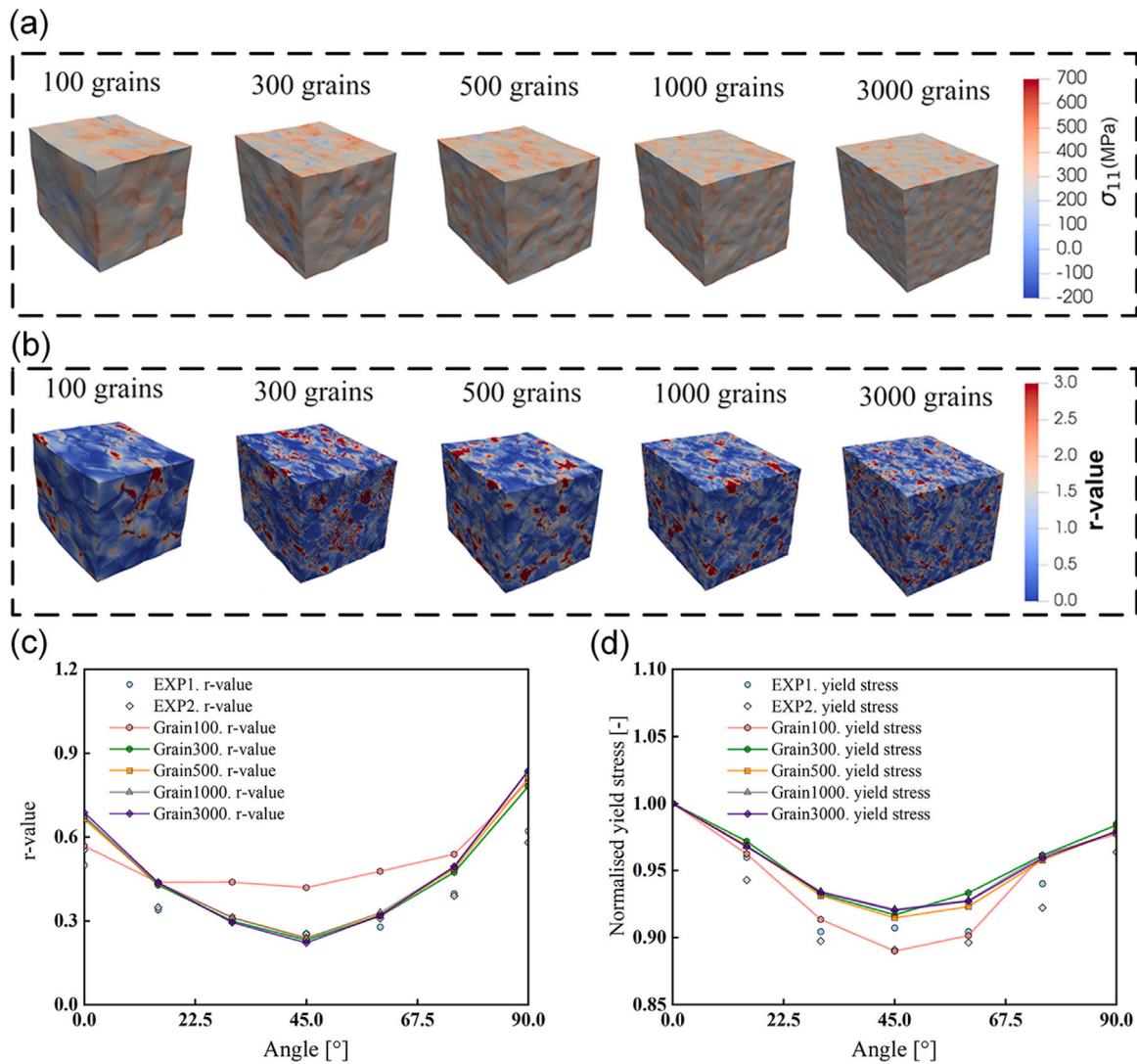
Fig. 7. The inhomogeneous distribution of (a) Cauchy stress component in loading direction and (b) r-value of each material point in the 3D RVEs with 100, 300, 500, 1000 and 3000 grains predicted by full-field CP simulations during the uniaxial tensile tests in RD at strain level of 0.1. (c) r-value versus angle from RD and (d) normalized yield stress versus angle from RD of the AA6016-T4 aluminium alloy predicted by the CP modelling utilizing the RVEs with 100~3000 grains in comparison with the experimental data (blue symbols).

0.09, to define the contact friction between the sheet and dies under lubrication. Here, five groups of constitutive models were used and compared in FE modelling and simulation to describe the complex anisotropic behaviour as well as to examine their prediction accuracy including:

(1) Physical tests based Yld2000-2d yield function denoted as Exp. Yld2000-2d

(2) Physical tests based Yld2004-18p yield function denoted as EXP. Yld2004-18p

(3) Virtual tests based Yld2000-2d yield function denoted as CP. Yld2000-2d

(4) Virtual tests based Yld2004-18p yield function denoted as CP. Yld2004-18p

(5) Evolving texture and anisotropy evolution based Yld2004-18p yield function denoted as TexEvo. Yld2004-18p

For the (1)~(4) models, the parameters of the yield function keep constant throughout the deep drawing simulations. For the TexEvo. Yld2004-18p, the local texture and yield function parameters are regularly updated at increment size of 0.05 equivalent plastic strain following the deformation path during the deep drawing simulations. In addition, to save computational cost, the resolution of the RVEs was adopted in TexEvo. Yld2004-18p model is defined as 40^3 Fourier points

since the plastic anisotropy prediction is converged when the resolution exceeds 32^3 as stated in Section 3.1.

4. Results and discussion

In this Section, the results of the virtual tests are thoroughly validated by the data of the experimental mechanical tests, such as normalized yield stress and r-value in uniaxial tests, biaxial yield points and plastic strain rates in RD-TD plane, hardening curve in shear and reverse shear tests. The evolution of the texture and plastic anisotropy at various positions during deep drawing is investigated using the evolving texture based multi-scale modelling, showing that, compared with the conventional approach with constant yield surface, the evolution of yield surface presents a considerable effect on the accuracy of the sheet metal forming simulations.

4.1. Experimental validation of virtual tests

In the CP-based virtual tests, the crystal structure of the AA6016-T4 aluminium sheet was set as FCC. In the CP model, 12 slip systems in FCC-structured metals, including $\{110\}\langle 111\rangle$ and the equivalent systems, were considered. The hardening behaviour was modelled by
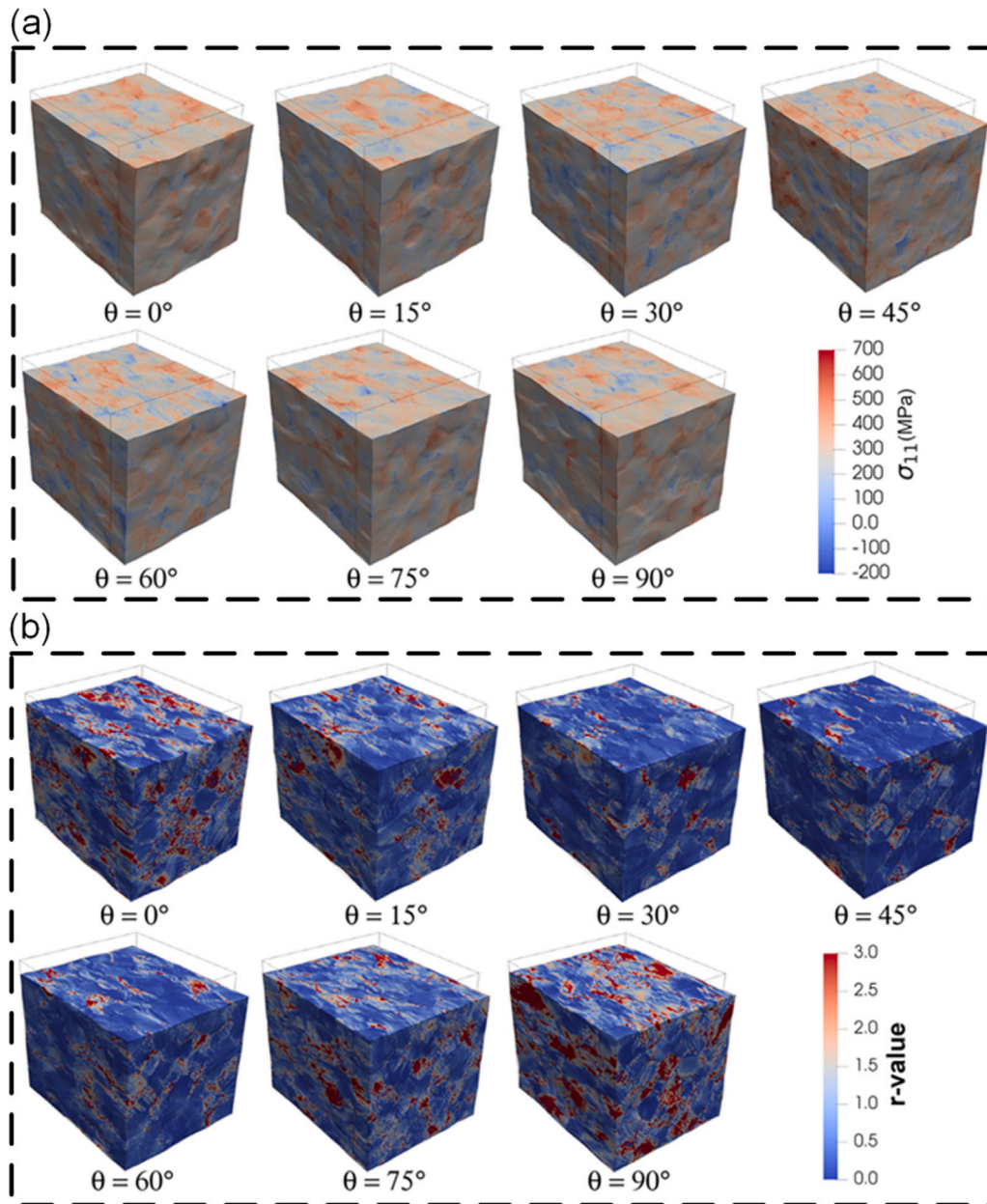
Fig. 8. (a) The inhomogeneous distribution of Cauchy stress component in loading direction and (b) r-value in each material point of the 3D RVE predicted by full-field CP simulations during the uniaxial tensile tests at strain level of 0.1 from RD to TD an interval of 15° compared with the initial shape of the RVE as denoted as the black outline. A pronounced inhomogeneity in the inter-granular and intra-granular stress distribution and the grain orientation dependent plastic deformations are captured.
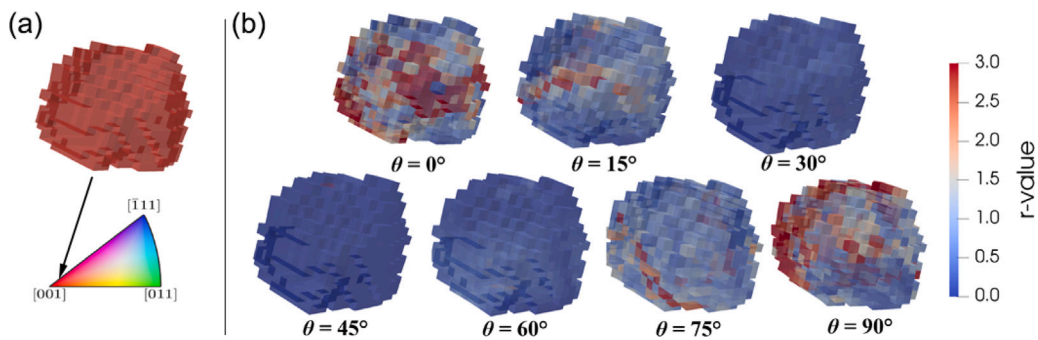

Fig. 9. (a) A near-cube orientation grains inside the RVE (the Euler angles is [1.69°, 9.33°, 0.57°]); (b) the distribution of r-value in each material point of this near-cube orientation grains during the virtual uniaxial tensile tests at strain level of 0.1 from RD to TD an interval of 15°. The intra-grain micromechanical field value is captured and the r-value in 45° is lower while in RD and TD is higher, which is in agreement with the feature of cube orientation.
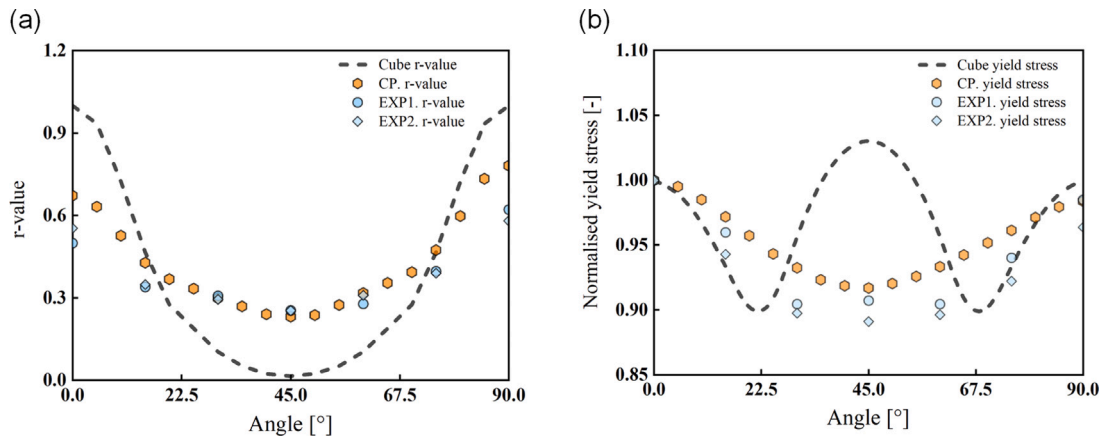
Fig. 10. (a) The r-value versus angle from RD and (b) normalized yield stress versus angle from RD of the AA6016-T4 aluminium alloy. The blue symbols are experimental data. The orange symbol is the result obtained from the virtual uniaxial tests. The black dashed line is the variation of the r-value and normalized yield stress of a single cube crystal.

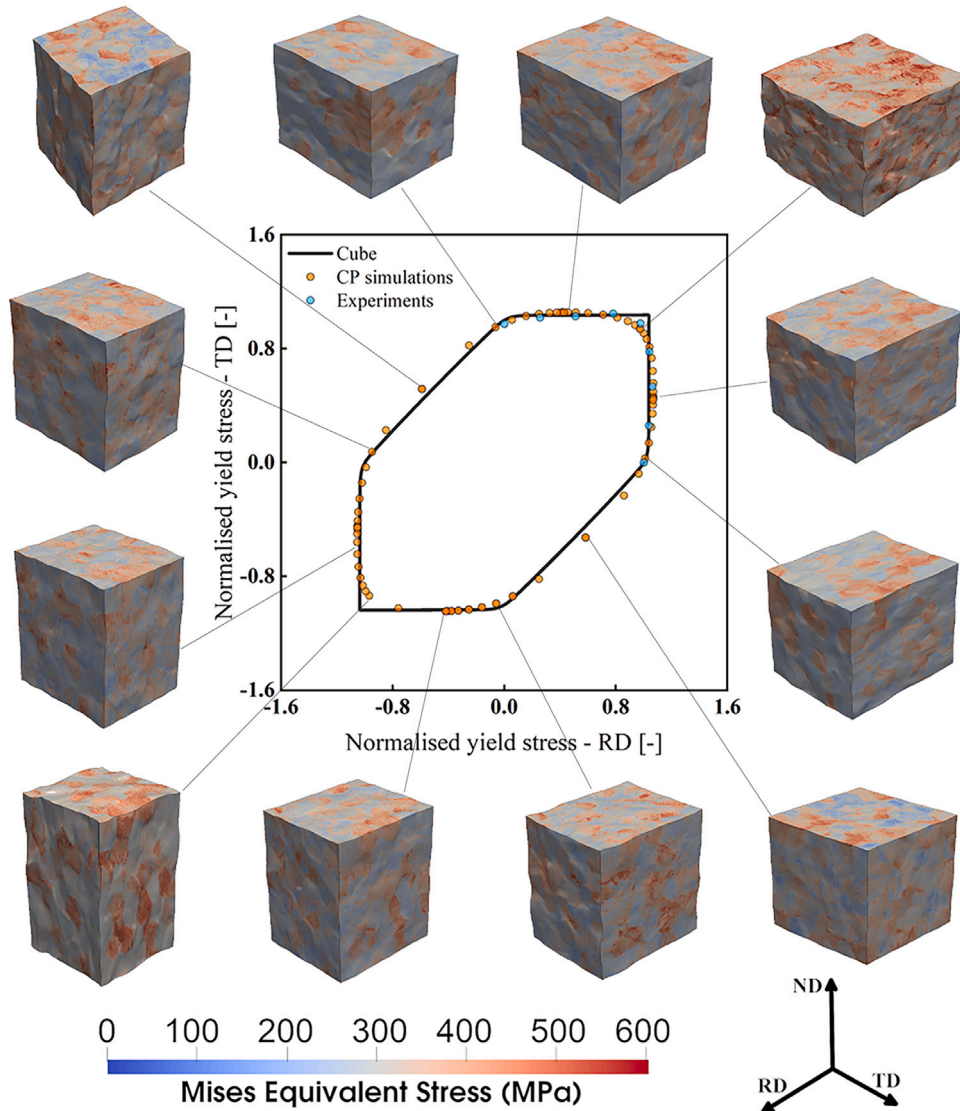**Fig. 11.** The distribution of Mises equivalent stress of the 3D RVEs in various virtual tests with different stress ratios in RD and TD at the equivalent strain level of 0.1. The corresponding virtual tests predicted normalized yield stress points are plotted in the RD-TD plane to compare with the experimental biaxial tensile tests results and the yield surface predicted by the single cube crystal plasticity modelling.
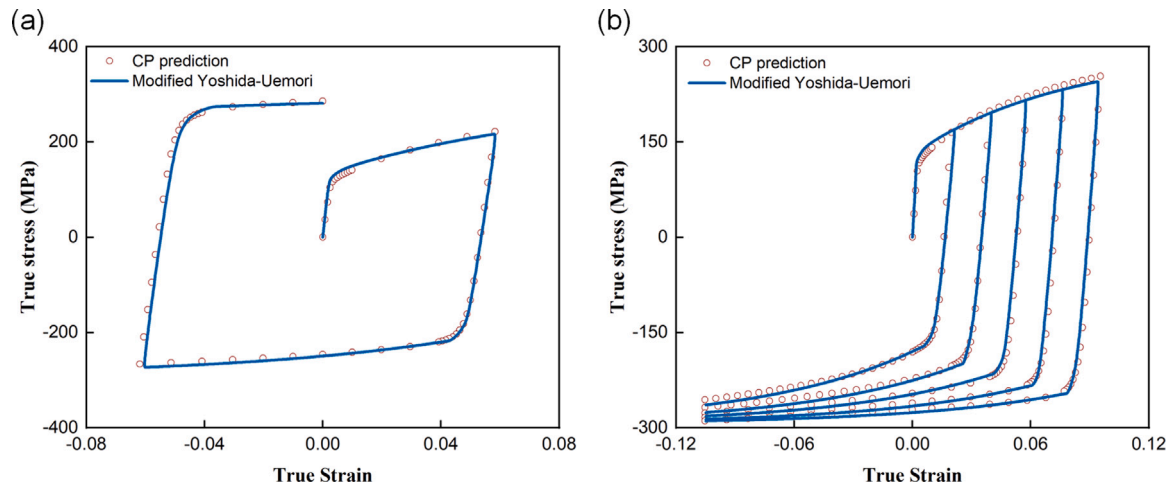
Fig. 12. (a) The comparison of true stress versus true strain response of AA6016-T4 during 1.5 cycles of uniaxial tension and reverse compression tests obtained by CP simulations and modified Yoshida–Uemori model (b) The true stress versus true strain response during 5 cycles of uniaxial tension and reverse compression tests obtained by CP simulations and modified Yoshida–Uemori model.
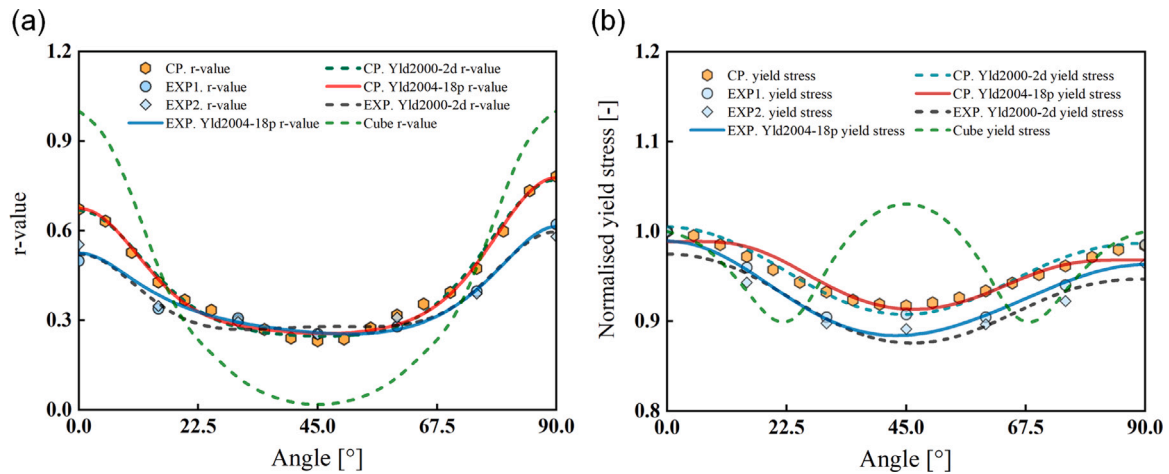

Fig. 13. (a) The r-value versus angle from RD and (b) normalized yield stress versus angle from RD of the AA6016-T4 aluminium alloy. The blue symbols are experimental data. The orange symbol is the result obtained from the virtual uniaxial tests. The dark cyan dot line and solid red line are the predicted results of the virtual tests based Yld2000-2d and Yld2004-18p yield functions. The black dot line and solid blue line are the predicted results of the physical tests based Yld2000-2d and Yld2004-18p yield functions. The olive dot line is the result obtained from single cube crystal plasticity modelling.

using a power law. The constitutive parameters used in the CP model are determined by an iterative global optimization scheme using the experimental results. The obtained material parameters of the CP model are given in Table 1. A comparison between stress–strain curves predicted by the CP modelling and experimental ones is demonstrated in Fig. 6. It can be observed that the CP model can well capture the stress–strain curves for both uniaxial tension and shear tests.

The CP model with the calibrated material parameters was further used to characterize the anisotropic plastic deformation of the AA6016-T4 sheet. For this purpose, a series of RVE-based virtual tests were carried out for exploring the material response under uniaxial tension in various directions with respect to RD. To investigate the effect of the number of grains adopted in RVE on the prediction of the plastic anisotropy, the five RVEs with 100∼3000 grains plotted in Fig. 4 were utilized to perform the virtual uniaxial tension under the loading direction in RD. Fig. 7a and b, respectively, indicate the distribution of Cauchy stress components σ_{11} and the r-value under loading direction in RD for the five RVEs at the strain level of 0.1. The variation of the CP modelling predicted r-value and normalized yield stress in various directions using 100∼3000 grains are illustrated in Fig. 7c and d, respectively. The plastic anisotropy prediction converges when the grain number exceeds 300. Therefore, the 300 grains are enough to

represent the texture of AA6016-T4 obtained from ODF data. In this work, the RVE with 300 grains is selected for all the virtual tests of AA6016-T4 to ensure a high resolution of each grain.

Fig. 8a show the distribution of Cauchy stress components in various loading directions of the 3D RVE with 300 grains during the virtual uniaxial tensile tests at the strain level of 0.1. It can be seen that the high-resolution CP simulations depicted the highly inhomogeneous stress field, which is an important feature of plastically deformed polycrystals. Such results indicate that the grain morphology and the crystallographic texture of the AA6016-T4 can lead to a pronounced inhomogeneity in the stress distribution at both inter-granular and intra-granular levels.

To further investigate the inhomogeneous deformation of the material, the r-values (represented as the strain rate ratios of TD-ND) of each material point under various loading modes were analysed, as shown in Fig. 8b. It can be observed that the textured polycrystals present significantly inhomogeneous plastic deformation. The full-field CP simulations reveal that not only the inter-granular but also intra-granular plastic deformation are inhomogeneous. In addition, the grain orientation dependent plastic deformations were captured by the full-field CP simulations, where the r-values of most material points are lower in 45° compared with the ones in RD and TD. This is because
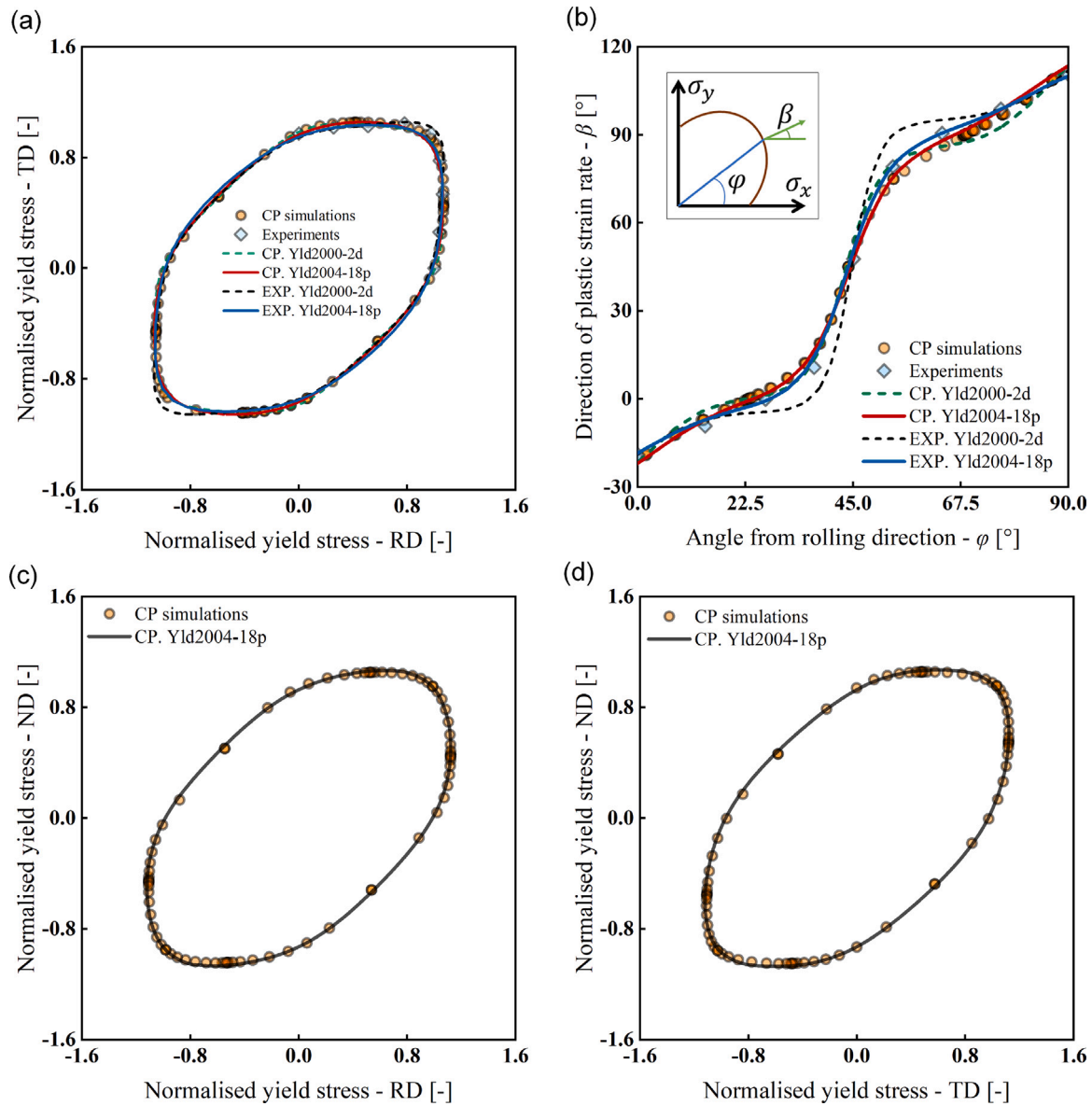
Fig. 14. (a) Yield surfaces ($\sigma_{12} = 0$) and (b) direction of plastic strain rate β versus angle of the stress ratio φ of the AA6016-T4 aluminium alloy in RD-TD plane. (c) Yield surfaces ($\sigma_{13} = 0$) in the RD-ND plane and (d) yield surfaces ($\sigma_{23} = 0$) in the TD-ND plane. The symbols"◊" are the experimental data. The symbols "○" are the material sampling points obtained from the virtual tests. The green dot line and red solid line are the predicted results of the virtual tests based Yld2000-2d and Yld2004-18p yield functions. The black dot line and blue solid line are the predicted results of the physical tests based Yld2000-2d and Yld2004-18p yield functions.

that AA6016-T4 presents a very strong cube texture. To clearly show the intra-granular plastic deformation of cube textured polycrystals, a single crystal with orientation [1.69°, 9.33°, 0.57°] (near the cube orientation [0°, 0°, 0°]) were taken from the RVE, and also the r-value distribution was illustrated in Fig. 9. As shown in this figure, the average r-value presents a lower level in 45°, which is similar to the plastic deformation characteristics of a material with the cube orientation. The Cauchy stress and r-value of all material points in RVEs are taken on average to obtain the macroscopic yield stress and the r-value. Fig. 10a and b show the macroscopic mechanical response predicted by full-field CP modelling and single cube crystal plasticity modelling in comparison with experimental data with respect to the variation of r-value and normalized yield stress, respectively. The prediction of the full-field polycrystalline CP modelling shows a similar plastic anisotropy feature with the single cube orientation and a good agreement with experiments.

Furthermore, the CP simulations of the biaxial test with various deformation rate ratios between RD and TD were conducted to identify

Table 2
The parameters of the modified YU model for the AA6016-T4 sheet.

y (MPa)	b_0 (MPa)	γ_1	c_2 (MPa)	γ_2	Q (MPa)	b	h
101.2	105.3	850	25.2	391.3	158.3	12.8	0.18

the yield surface of AA6016-T4. Fig. 11 shows the virtual tests in the various cases of virtual biaxial tests, where the inhomogeneous distribution of Mises equivalent stress was depicted by the full-field CP simulations. Also, it can be seen that the intra-granular stress field is significantly inhomogeneous in the biaxial loading cases.

The experimental results have proven that the inter-granular and intra-granular plastic deformation of polycrystals is highly inhomogeneous since the mechanical response of crystal structure is dependent on the axis between grain orientation and loading direction [82]. Therefore, the inhomogeneous micromechanical field values of the deformed polycrystals are determined by the crystallographic texture and grain morphology. In this work, the EBSD-based RVEs are capable

Table 3

The parameters of AA6016-T4 aluminium alloy for Yld2000-2d model.

Yld2000-2d coefficients determined by virtual tests (exponent a = 8):

α_1	α_2	α_3	α_4	α_5	α_6	α_7	α_8
0.913721	1.061592	1.158090	1.050692	1.024416	1.033475	0.902132	1.314560

Yld2000-2d coefficients determined by physical tests (exponent a = 8):

α_1	α_2	α_3	α_4	α_5	α_6	α_7	α_8
0.894773	1.059962	0.908823	1.047906	1.033545	0.906414	0.786078	1.486544

Table 4

The parameters of AA6016-T4 aluminium alloy for Yld2004-18p model.

Yld2004-18p coefficients determined by virtual tests (exponent a = 8):

α_1	α_2	α_3	α_4	α_5	α_6	α_7	α_8	α_9
1.398018	0.964117	0.559008	0.650067	0.730785	−0.237217	1.393686	1.058119	0.854854
α_{10}	α_{11}	α_{12}	α_{13}	α_{14}	α_{15}	α_{16}	α_{17}	α_{18}
1.006173	0.177381	0.487335	0.319294	1.271040	1.561203	0.392646	0.494739	0.714556

Yld2004-18p coefficients determined by physical tests (exponent a = 8):

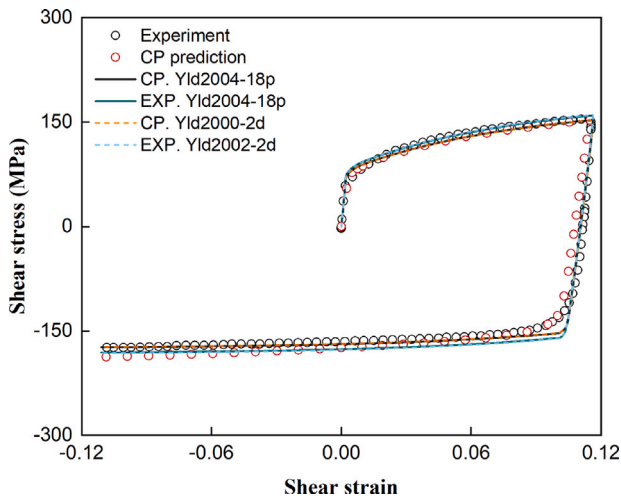| α_1	α_2	α_3	α_4	α_5	α_6	α_7	α_8	α_9
0.463447	0.744861	0.394319	0.529571	0.298255	−0.375017	1.237525	1.000000	1.000000
α_{10}	α_{11}	α_{12}	α_{13}	α_{14}	α_{15}	α_{16}	α_{17}	α_{18}
0.700466	−0.858842	0.798784	−0.654461	−0.739708	0.589553	0.390343	1.000000	1.000000

Fig. 15. The comparison of true stress versus true strain response of AA6016-T4 during 1.5 cycles of shear tension and reverse shear tests obtained by physical tests, CP simulations and CP. Yld2004-18p, EXP. Yld2004-18p, CP. Yld2000-2d and EXP. Yld2000-2d combined with the modified Yoshida–Uemori model. The cyclic hardening behaviour in the shear and reverse shear tests are successfully captured by the virtual tests and the multi-scale modelling scheme.

of mapping such inhomogeneities caused by the strong cube texture and the grain morphology of AA6016-T4. Hence, these full-field CP simulations can provide a more authentic description of the micromechanical responses of AA6016-T4 in various uniaxial and biaxial loading cases. Furthermore, the CP predicted mechanical anisotropy at the engineering length scale is determined from the average of the stress and strain of all material points. If a small number of grains were used in RVE, the significant difference in deformation may lead to a relatively greater scatter of predicted yield stresses. However, the 300 grains used in the RVE could obviously reduce the statistical discrepancy and improve the accuracy of prediction in mechanical anisotropy at the engineering length scale.

To provide a more synthetical study on the mechanical anisotropy of AA6016-T4, more plastic deformation modes were taken into account in the virtual tests, including tension–compression, shear and reverse shear, uniaxial tension in the directions from RD to TD at intervals of 5°, and biaxial tension of 80 material sampling points in the RD-TD, RD-ND and TD-ND planes. After that, the virtual testing results and experimental testing results were compared to evaluate the prediction capability of CP simulations.

As indicated in Fig. 12a, the stress–strain response in the uniaxial tension–compression test in RD (1.5 cycles) predicted by CP simulation was used to identify the parameters of the modified YU kinematic hardening model, and the identified parameter values are documented in Table 2. To evaluate the performance of the calibrated hardening model in various strain levels, a comparison between the stress–strain curves predicted by CP simulation and YU model for the five tension–compression cycles was plotted in Fig. 12b. It can be found that the calibrated YU hardening model can well capture the tension–compression full-history stress–strain response.

Fig. 13a and b respectively show the r-values and yield stresses of virtual and physical uniaxial tensile tests at a nominal strain of 0.1 from 0° to 90° at an interval of 5°. Both virtual and physical results show that the r-value is relatively higher at 0° and 90° but lowest at 45°. In addition, the lowest normalized yield stress is also observed at 45° which is about 0.90 and 0.92 obtained from physical and virtual experiments, respectively. It is noted that although the variation of r-value and yield stress predicted by virtual experiments is similar to physical experiments, the values are relatively higher in each direction. Due to the strong cube texture as observed in the EBSD map (shown in Fig. 3), the variation of the r-value and yield stress for a single cube crystal was plotted as reference (obtained by single crystal plasticity modelling). It is seen that mechanical anisotropy obtained by physical tests is closer to the single cube crystal compared with virtual tests.

The anisotropy properties obtained from experiments and virtual tests were used to calibrate the parameters of Yld2000-2d and Yld2004-18p yield functions. The Levenberg–Marquardt least square method was employed to optimistically identify these model parameters, and the obtained values of these parameters are stated in Tables 3 and 4. As illustrated in Fig. 13a and b, the uniaxial r-values and yield stresses in various directions obtained by experimental and virtual tests are successfully captured by corresponding EXP. Yld2000-2d, EXP. Yld2004-18p, CP. Yld2000-2d and CP. Yld2004-18p models, respectively. It needs to be noted that the initial parameters of the TexEvo. Yld2004-18p is same as CP. Yld2004-18p, but the parameters will be regularly recalibrated by the virtual tests using the evolving texture with the increasing of plastic deformation level.

The yield stresses under biaxial tension as well as the plastic strain rate in the RD-TD plane are demonstrated in Fig. 14a and b, respectively. As compared with the experimental results, the virtual biaxial tests successfully predict yield locus in the biaxial tensile stress state. Moreover, the yield stress points in tension–compression and compression–compression stress states can also be well captured by the virtual tests. However, such complex material responses are still a challenge to be obtained through physical tests. For the plastic
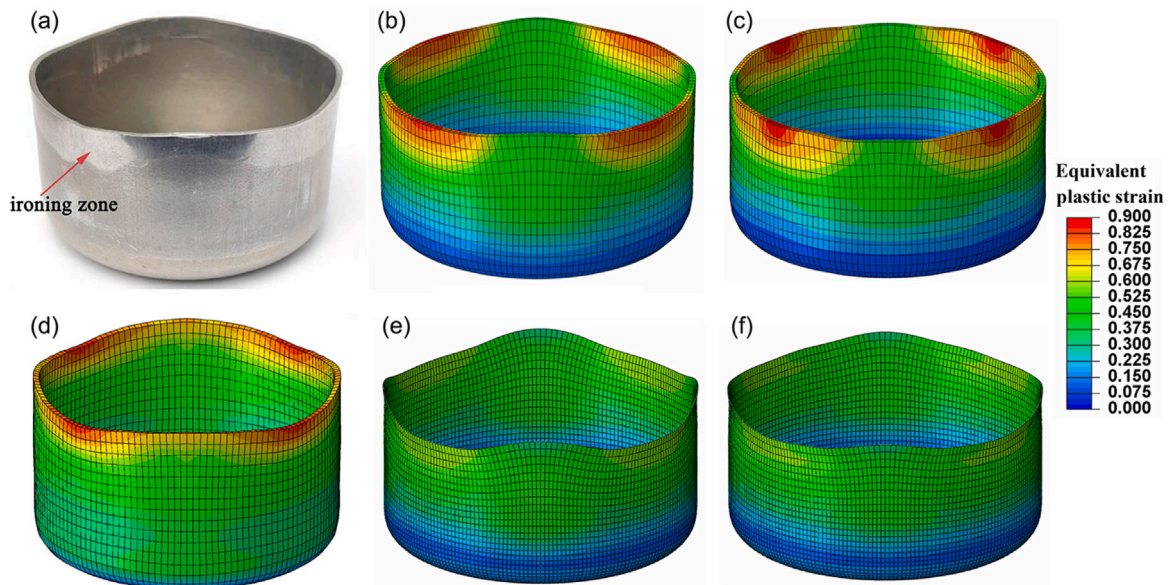
Fig. 16. (a) The experimental drawn cylindrical cup of AA6016-T4 with four "ears" and an ironing zone (due to the small tooling clearance) is observed at the top wall. The corresponding simulated earing configuration and equivalent plastic strain contours of the drawn cups were obtained from the five groups of models: (b) CP. Yld2004-18p, (c) EXP. Yld2004-18p, (d) TexEvo. Yld2004-18p, (e) CP. Yld2000-2d, (f) EXP. Yld2000-2d models.

deformation mode in biaxial tension, the virtual tests also give an accurate prediction in the plastic flow direction (Fig. 14b). Compared with those properties of single cube texture, both virtual and physical tests depicted the feature of yield surface of cube texture, e.g. the axis of symmetry is 45 degrees and a right angle is located at the equibiaxial stress point (shown in Fig. 11). Moreover, for the direction of plastic strain rate in various stress ratios, the results obtained from physical tests are closer to those obtained from the single cube crystal.

For the calibration of advanced 3D phenomenological yield function, the out-of-plane mechanical anisotropy is also needed so the virtual tests are also used to predict the yield stresses of the biaxial loading in the RD-ND (Fig. 14c) and TD-ND planes (Fig. 14d). These material sampling points are utilized to determine the out-of-plane parameters $\alpha_8, \alpha_9, \alpha_{17}$ and α_{18} of CP. Yld2004-18p. Since the physical uniaxial and biaxial experiments were only conducted in the RD-TD plane, the out-of-plane parameters $\alpha_8, \alpha_9, \alpha_{17}$ and α_{18} of EXP. Yld2004 were assumed as one [17]. As indicated in Fig. 14, the virtual tests predicted biaxial material sampling points in the RD-TD plane are successfully captured by corresponding CP. Yld2000-2d and CP. Yld2004-18p models and the experimental ones are accurately described by the EXP. Yld2000-2d, EXP. Yld2004-18p. In addition, CP. Yld2004-18p also accurately describes the out-of-plane mechanical anisotropy in RD-ND and TD-ND planes.

Furthermore, to evaluate the performance of various yield functions associated with the modified Yoshida–Uemori model, the shear-reverse shear stress–strain responses obtained by various phenomenological models, CP predictions and experiments were plotted in Fig. 15. It can be seen that the virtual uniaxial tension–compression tests calibrated hardening models incorporated with various yield functions are capable of accurately predicting the mechanical response of AA6016-T4 in the shear-reverse shear deformation mode.

The above analysis demonstrates that the CP-based virtual tests could successfully predict the initial mechanical anisotropy in various deformation modes particularly in these modes that can be difficult or even not be done in physical experiments. Therefore, these virtual tests could provide an appropriate substitute for physical tests to investigate the initial yield behaviour in more complicated stress states at the grain-length scale. However, unavoidable deviations in the prediction of mechanical anisotropy do exist. These deviations could be attributed to several possible sources, including (i) inhomogeneity of various

regions selected for microstructure characterization, (ii) the microstructure information of 3D RVE is generated from the EBSD mapping in RD-TD plane without consideration of out-of-plane microstructure in thickness direction and (iii) the periodical boundaries of virtual experiments are not fully consistent with physical tests.

The five groups of the constitutive models developed in this study have been numerically implemented into ABAQUS (standard solver) through the UMAT subroutine, which would be used to perform the cylindrical cup drawing simulations.

4.2. Simulations of cylindrical deep drawing tests

According to the previous work [83], four ears located at 0°, 90°, 180° and 270° were normally observed in the cylindrical cup drawing of aluminium sheet with the single cube crystal structure. Essentially, this phenomenon is attributed to the higher r-value at RD and TD and lower r-value at DD (diagonal direction) in cube crystal [84]. Fig. 16 shows the distribution of equivalent strain in the drawn cup predicted by different models, including CP. Yld2004-18p, EXP. Yld2004-18p, TexEvo. Yld2004-18p, CP. Yld2000-2d and EXP. Yld2000-2d. It can be seen that the strain of the "peak" at the top edge is lower, while the "valley" is greater due to the anisotropic plastic deformation. The shape of the drawn cup part is predicted by TexEvo. Yld2004-18p and CP. Yld2004-18p model well agrees with the experimental results, while the ear variations predicted by CP. Yld2000-2d and EXP. Yld2000-2d is overestimated. Fig. 17a shows the experimental and simulated earing profiles, where the four ears located at 0°, 90°, 180° and 270° are observed in experimental cup part due to the very strong cube texture. It is seen that TexEvo. Yld2004-18p model, which is involved with the texture and plastic anisotropy evolution, presents the superior accuracy of the earing profile prediction than the other four conventional models, which keep the constant yield surface throughout the simulations.

Since the ironing process occurs at the top zone of the drawn cup wall (seen in Fig. 16a), the plastic deformation in the thickness direction is fully constrained, i.e., the plastic deformation in this zone fully flows toward the direction of cup height. Therefore, the accuracy of cup-wall thickness prediction is essential for the earing profile prediction, because it determines the volume of the material flowing toward the direction of cup height. Fig. 17b shows the thickness distribution
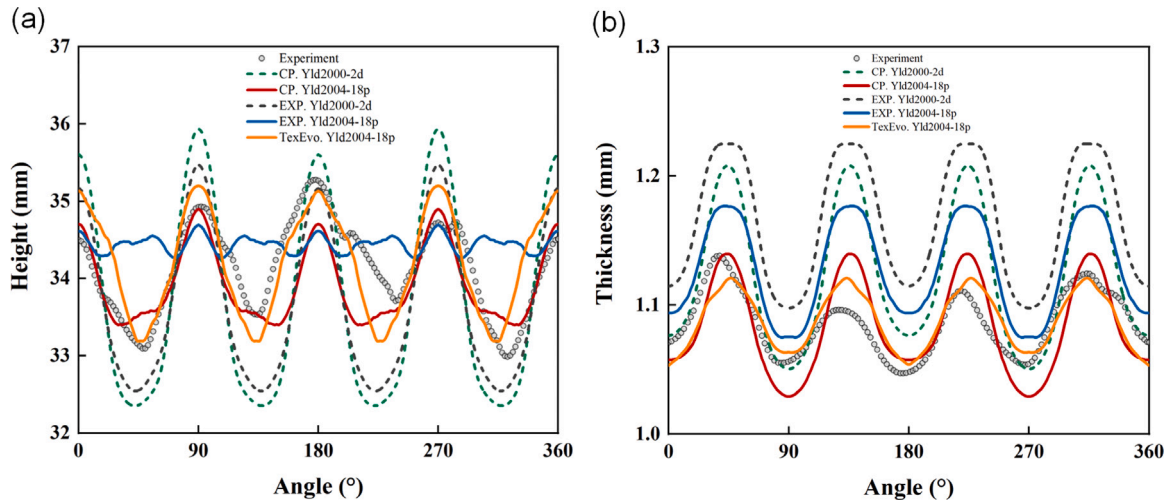
(a)

(b)

Fig. 17. (a) The experimental and five groups of simulations predicted earing profiles, where the four ears located at 0°, 90°, 180° and 270° are observed in experimental cup part due to the very strong cube texture. The evolution of anisotropy can have a considerable effect (considering in the TexEvo. Yld2004-18p) on the prediction accuracy of the earing profiles. (b) The distribution of wall thickness along 20 mm cup height of the drawn cylindrical cups that were obtained from experiments and five groups of simulations. The evolution of anisotropy also has a significant effect on the prediction accuracy of the plastic deformation in the thickness direction.
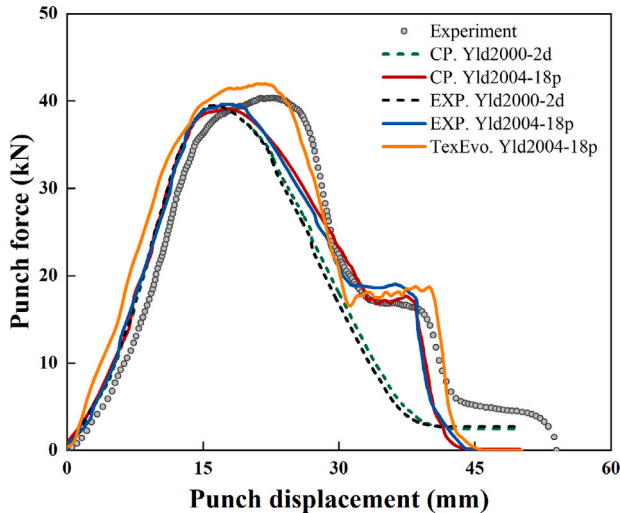

Fig. 18. The experimental punch force versus displacement curve during the deep drawing process in comparison with the prediction in five groups of simulations. For the conventional approaches with constant yield surface, the predicted force underestimates the actual punch force in experiments when it exceeds the peak point. The evolving texture based TexEvo. Yld2004-18p significantly improve the accuracy in the loading history prediction.

of the formed cup part at the location with a cup height of 20 mm. It can be observed that the thickness predicted by TexEvo. Yld2004-18p and CP. Yld2004-18p can well agree with the experiments, presenting a superiority over other models due to the out-of-plane plastic anisotropy that is considered in these models. Therefore, the TexEvo. Yld2004-18p and CP. Yld2004-18p accurately predict the plastic deformation during the ironing process, which leads to the accurate prediction in the earing profile. The EXP. Yld2004-18p provides an overestimation of the thickness of the formed cup part in DD, and hence gives more volume of the material flowing toward the direction of cup height during the ironing process, which resulted in the overestimation of cup height prediction in DD. For the in-plane stress model CP. Yld2000-2d and EXP. Yld2000-2d using shell element, the ears height is significantly overestimated because the ironing process is not captured in simulations. In addition, there is little difference in the earing profile prediction of the CP. Yld2000-2d and EXP. Yld2000-2d model, because the in-plane plastic

anisotropy predicted by virtual tests is in good agreement with the physical tests, which plays the dominant role in the computation of the plastic deformation in the in-plane stress model.

Furthermore, the prediction capability for forming force is also analysed. Fig. 18 compares the predicted punch force with the experimental one. It can be found that the TexEvo. Yld2004-18p predicted forces well agree with the experiment during the entire deep drawing process. For the other four models, the peak value of punch forces obtained from the simulations is similar to that in the experiment, but the peak point occurs prior to that in the experiment. When it exceeds this peak point, the predicted force, however, underestimates the actual punch force in experiments. In addition, a plateau similar to the experimental one for punch displacements between 33 and 38 mm can be observed in the results of TexEvo. Yld2004-18p, CP. Yld2004-18p and EXP. Yld2004-18p models, while this phenomenon is not noticed in CP. Yld2000-2d and EXP. Yld2000-2d models. This plateau is attributed to the ironing during forming, which can be described by using 3D solid elements but not shell elements.

In summary, the TexEvo. Yld2004-18p model provides a better prediction in earing profile, wall thickness variation and punch loading history of the drawn cup because the texture evolution and the induced evolving plastic anisotropy are taken into account in the large plastic deformation simulations, which is more realistic as the actual experiments. However, it must be noted that regular texture updating and virtual tests are highly time-consumption. Here, a deep drawing simulation is employed using the updated increment size of 0.05 equivalent plastic strain. The corresponding computational time is 52 h using 256 threads on a high-performance workstation with dual AMD 7T83 CPUs. In addition, only 1.5 h and 0.2 h are consumed in the conventional approach using the constant parameters of Yld2004-18p and Yld2000-2d yield functions. Therefore, the set-up of the resolution of the RVEs and the updated increment size is very sensitive to the computational cost when this scheme is applied to the forming simulations of real automotive parts with a much larger size.

4.3. Texture evolution in deep drawing

To show the local texture evolution predicted by the TexEvo. Yld2004-18p, the local texture of the material points at the 9 positions on the final deep drawn cup in comparison with the initial texture are illustrated in Fig. 19. It is seen that the different local plastic strain paths and plastic deformation levels lead to a different texture
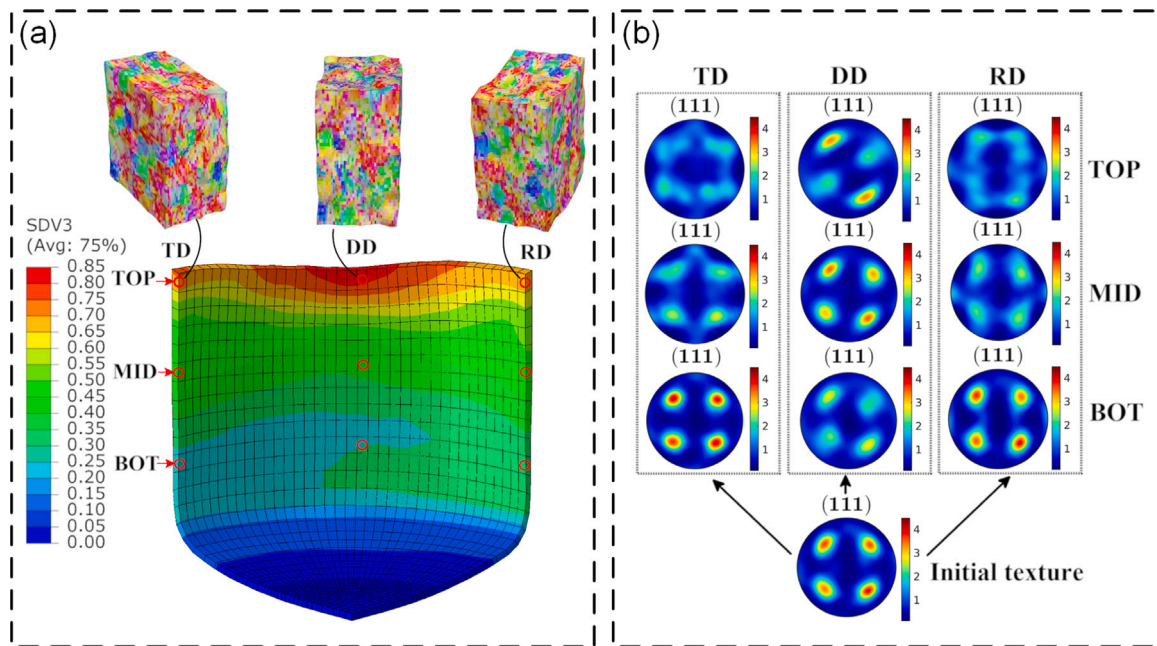
Fig. 19. TexEvo. Yld2004-18p model predicted (a) distribution of equivalent plastic strain of deep drawn cup and the texture of three deformed RVE with IPF colour mapped at three positions RD-TOP, DD-TOP and TD-TOP on the cup edge. (b) The local evolving texture after deep drawing tests plotted by (111) pole figures at 9 different positions in deep drawn cup compared with AA6016-T4 initial texture, where a significant and different texture evolution is observed at various positions experienced different strain paths.
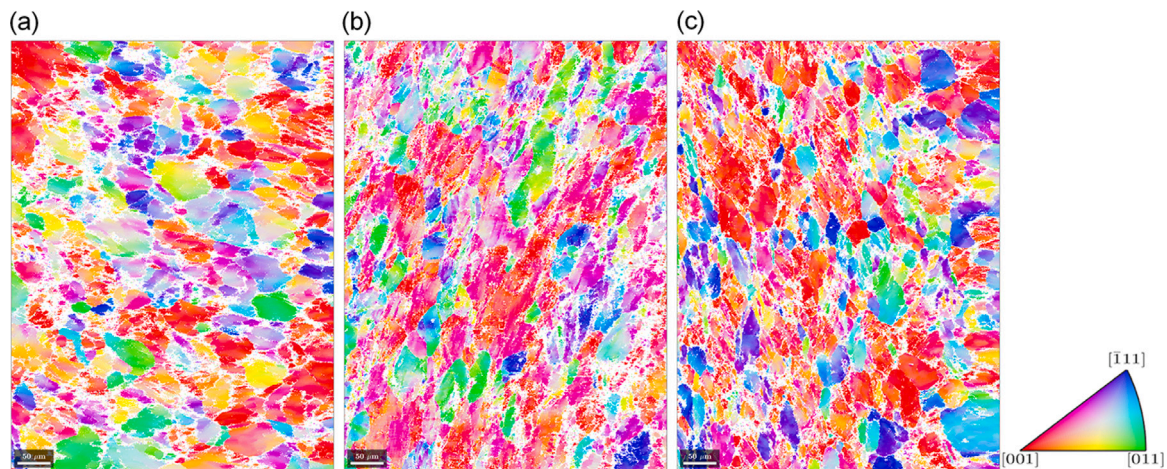

Fig. 20. The microstructure characterization in terms of crystalline morphology and texture after the large plastic deformation is conducted utilizing the EBSD scanning IPF map on the three specimens cut from the deep drawn cup at the three positions on the top of the cup wall (a) RD-TOP, (b) DD-TOP and (c) TD-TOP. The texture data is used for the validation of evolving texture based multi-scale modelling.

evolution, especially at RD-TOP, DD-TOP and TD-TOP where the intensity of the cube texture is reduced. Additionally, to verify the texture prediction at these three points, the EBSD tests are conducted on the corresponding area cut from the experimental drawn cup. The EBSD maps of the RD-TOP, DD-TOP and TD-TOP are illustrated in Fig. 20 and the EBSD data generated (100) and (111) pole figures are plotted in Fig. 21. As a comparison, the TexEvo. Yld2004-18p modelling predicted local textures of the deformed RVEs at RD-TOP, DD-TOP and TD-TOP are also plotted as (100) and (111) pole figures in Fig. 21. It is seen from the pole figures, a good agreement of the deformed texture is achieved between the experimental measurement and modelling prediction at the three material points, which experienced different deformation paths. Therefore, the proposed TexEvo. Yld2004-18p model shows a good performance in the prediction of the local texture in the various complicated strain path.

4.4. Evolution of plastic anisotropy in deep drawing

The local texture evolution induced change of the directional uniaxial normalized yield stress, and r-value are investigated during the deep drawing simulations of the AA6016-T4 sheet. As illustrated in Fig. 22a, c and e, the different directional normalized yield stress evolution in various equivalent plastic strains are observed at the material points RD-TOP, DD-TOP and TD-TOP. A 'valley' at the angle of 30° is to level down with the increasing of the plastic deformation at the point RD-TOP. At point, DD-TOP, the level of a 'peak' at an angle of 20° and a 'valley' at the angle of 70° is gradually increasing with the increase of the equivalent plastic strain, and this evolution at point TD-TOP is similar to point DD-TOP. Fig. 22b, d and f show the directional r-value evolution at the material points RD-TOP, DD-TOP and TD-TOP, respectively. For the material point RD-TOP, the plastic anisotropy in
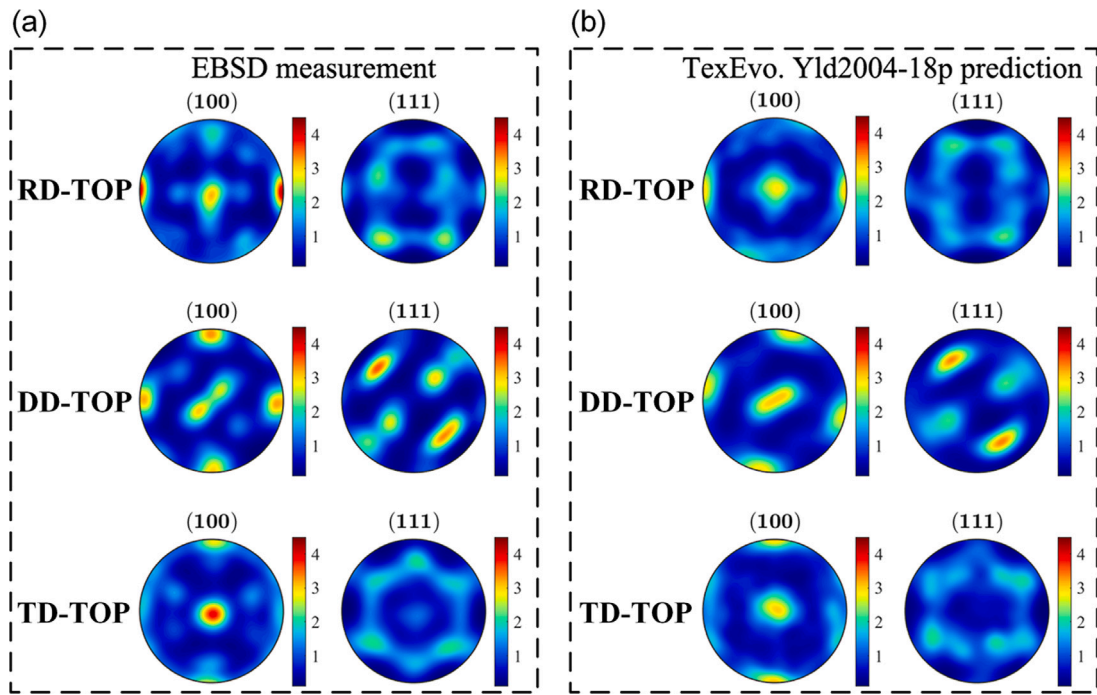
Fig. 21. (a) The pole figures in (100) and (111) orientations of the three positions RD-TOP, DD-TOP and TD-TOP at the cup top edge after deep drawing obtained from EBSD measurements. (b) The corresponding local texture illustrated as the pole figures in (100) and (111) orientations at the same positions predicted by evolving texture based multi-scale modelling. A good agreement of the deformed texture is achieved between the experiments and modelling prediction at the three positions, which experienced different strain paths.

the r-value is gradually reduced, i.e. the concave variation of the r-value progressively flattens with the increasing of the plastic deformation. A 'peak' at the angle of 75° gradually rises for the material point DD-TOP. At the material point TD-TOP, the r-value is gradually increasing at the range from 0° to 70°.

Based on the above results, the mechanical anisotropy obtained by the regularly updated texture based virtual tests is accurately passed to the yield function, hence the full-field CP modelling and the phenomenological yield function are successfully embedded in the multi-scale modelling scheme to take account of the evolving texture induced plastic anisotropy evolution.

5. Conclusions

In this work, a novel multi-scale computational framework is developed to simulate the evolving texture and it induced anisotropic plasticity evolution in metal forming, aiming to enhance the capability of forming simulations at an engineering-length scale. This computational framework consists of an FE model with advanced phenomenological yield functions and two-surface kinematic hardening model implemented, a spectral method based full-field CP model, as well as a cross-scale updating algorithm enabling real-time interaction of the FE model and CP model. Therefore, this approach enables the full-field CP modelling to be employed at engineering-length scale simulations without using homogenization schemes, the strain path dependent local texture and anisotropic plasticity evolution is successfully achieved in finite element analysis and only the initial texture is required as input data without extensive physical mechanical tests.

The developed multi-scale computational scheme involving the evolving texture is carefully validated in deep drawing tests using AA6016-T4 sheets with strong cube texture. The different evolving texture and corresponding yield surface evolution are observed at various positions of the drawn cup parts, which experienced different strain paths. Compared with the conventional approach assuming the constant yield surface shape, more accurate prediction of earing profile, wall thickness, loading history and texture evolution has been obtained by the evolving texture based scheme, i.e., the texture evolution has a considerable effect on simulation accuracy and should be taken account into the sheet metal forming simulations. Also, the numerical scheme presented in this work were presented in a general form, which can be associated with other CP constitutive model and advanced yield functions. Besides the deep drawing simulations, this scheme can be used in the optimization of the texture of different textured materials through various sheet metal forming simulations.

CRediT authorship contribution statement

Wencheng Liu: Conceptualization, Methodology, Investigation, Formal analysis, Writing – original draft, Writing – review & editing. **Jia Huang:** Investigation, Modelling, Formal analysis, Writing – review & editing. **Yong Pang:** Investigation, Modelling, Formal analysis, Writing – review & editing. **Ke Zhu:** Formal analysis, Writing – review & editing. **Shugen Li:** Formal analysis, Writing – review & editing. **Jun Ma:** Conceptualization, Methodology, Formal analysis, Writing – original draft, Writing – review & editing.

Declaration of competing interest

The authors declare that they have no known competing financial interests or personal relationships that could have appeared to influence the work reported in this paper.

Data availability

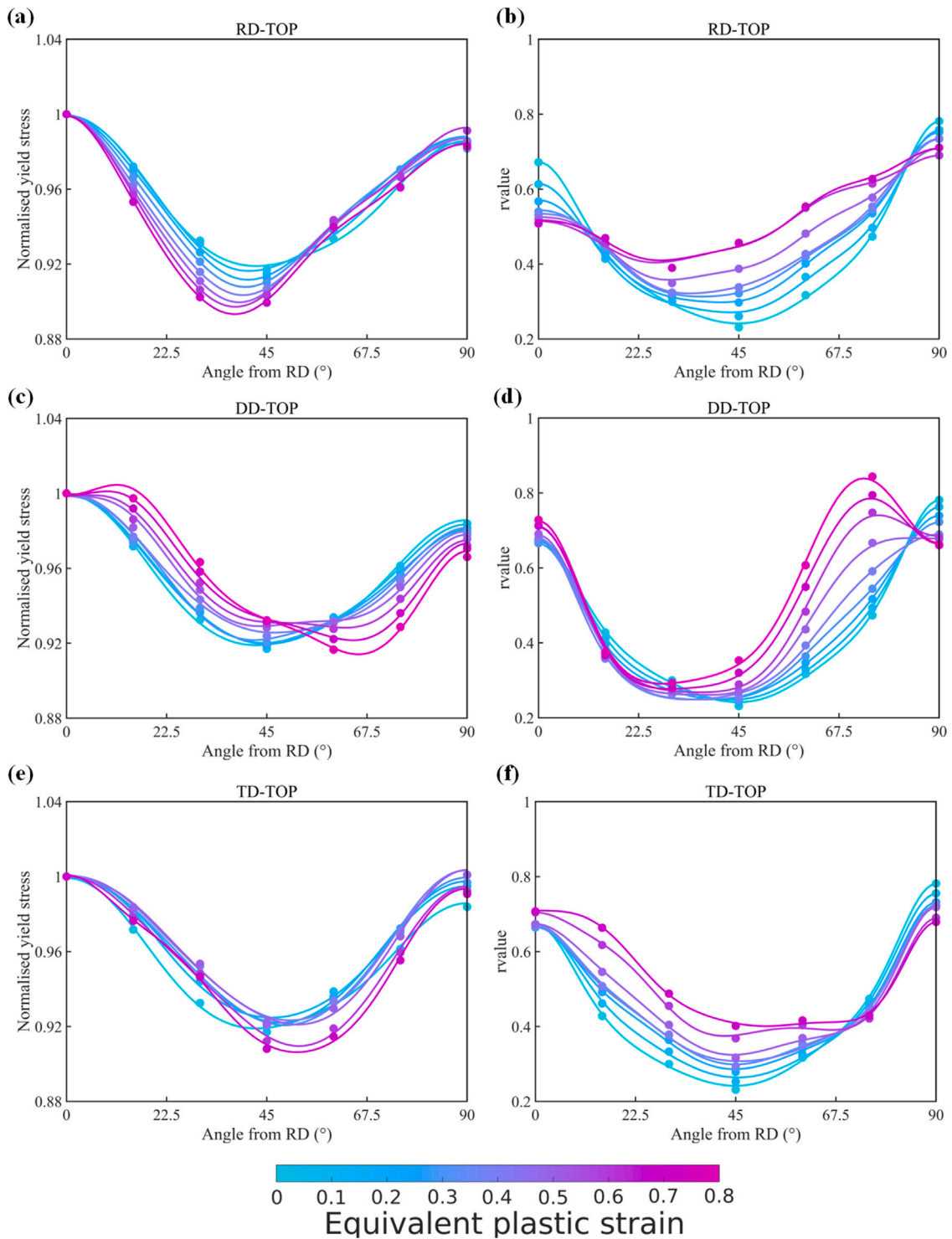Data will be made available on request.

Fig. 22. The continued evolution of normalized yield stress and r-value during the deep drawing process at the range of equivalent plastic strain from 0 to 0.8 at an interval of 0.1 predicted by the texture evolving based TexEvo. Yld2004-18p model started from AA6016-T4 initial texture at three different positions on the cup top edge: RD-TOP shown in figures (a) and (b); DD-TOP shown in figures (c) and (d); and TD-TOP shown in figures (e) and (f).

Appendix

In the spectral method, the numerical solution of RVE was calculated by complementary boundary conditions (BCs) in terms of deformation gradient $\bar{\mathbf{F}}$ and Piola–Kirchhoff stress $\bar{\mathbf{P}}$ [49,50]. As illustrated in Fig. 2, the deformation gradient history of each element in UMAT is employed as the periodical BCs of CP modelling to predict the texture evolution once the accumulated equivalent plastic strain exceeds the threshold. Here, the accumulated strain $\text{SDV}_{\epsilon_{ij}}$ tensor in UMAT divided by deformation time 100 s was adopted as the deformation gradient $\dot{\bar{\mathbf{F}}}$ given by,

$$\frac{\dot{\bar{\mathbf{F}}}}{10^{-2}\text{s}^{-1}} = \begin{bmatrix} \text{SDV}_{\epsilon_{11}} & \text{SDV}_{\epsilon_{12}} & \text{SDV}_{\epsilon_{13}} \\ 0 & \text{SDV}_{\epsilon_{22}} & \text{SDV}_{\epsilon_{23}} \\ 0 & 0 & \text{SDV}_{\epsilon_{33}} \end{bmatrix} \quad \text{and} \quad \frac{\bar{\mathbf{P}}}{\text{Pa}} = \begin{bmatrix} * & * & * \\ * & * & * \\ * & * & * \end{bmatrix} \quad (37)$$

Subsequently, virtual uniaxial, and biaxial tensile tests using the new texture were conducted to provide the plastic anisotropy data for the identification of the yield function. For the uniaxial tension along the RD, the deformation rate 1×10^{-2} s^{-1} was set in the $\dot{\bar{\mathbf{F}}}_{11}$ direction and the deformation rate of $\dot{\bar{\mathbf{F}}}_{22}$ and $\dot{\bar{\mathbf{F}}}_{33}$ would be adjusted to a value, which results in a zero Piola–Kirchhoff stress $\bar{\mathbf{P}}$ in these directions:

$$\frac{\dot{\bar{\mathbf{F}}}}{10^{-2}\text{s}^{-1}} = \begin{bmatrix} 1 & 0 & 0 \\ 0 & * & 0 \\ 0 & 0 & * \end{bmatrix} \quad \text{and} \quad \frac{\bar{\mathbf{P}}}{\text{Pa}} = \begin{bmatrix} * & * & * \\ * & 0 & * \\ * & * & 0 \end{bmatrix} \quad (38)$$

For the virtual uniaxial tensile tests along the angle θ from RD, an equivalent approach was used instead of rotating the BCs Eq. (38), in which the Euler angle of the orientations in RVE is rotated as $\{\phi_1 - \theta, \Phi, \phi_2\}$. For the case of virtual biaxial tensile tests, the different ratio of the deformation rate was applied in the RD and TD, while the deformation rate in ND will be adjusted to a value, which results in a zero Piola–Kirchhoff stress $\bar{\mathbf{P}}$ in ND directions. For instance, the BCs of the equibiaxial tensions are defined as:

$$\frac{\dot{\bar{\mathbf{F}}}}{10^{-2}\text{s}^{-1}} = \begin{bmatrix} 1 & 0 & 0 \\ 0 & 1 & 0 \\ 0 & 0 & * \end{bmatrix} \quad \text{and} \quad \frac{\bar{\mathbf{P}}}{\text{Pa}} = \begin{bmatrix} * & * & * \\ * & * & * \\ * & * & 0 \end{bmatrix} \quad (39)$$

Due to the high computational efficiency of spectral solver, the computations of these virtual tests using RVEs with a resolution of $40 \times 40 \times 40$ FOURIER points are parallel and they only take about 20 s to reach the deformation solutions at a plastic strain of 0.005 under 256 threads using a high-performance workstation with AMD EPYC 7763 $\times$ 2 128 cores CPUs. Once these virtual tests are completed, the stress tensor and plastic strain rate at a plastic strain of 0.005 were output to calculate the plastic anisotropy data including (i) normalized directional uniaxial yield stress $Y_u^{CP}(\theta)$ and r-value $r_u^{CP}(\theta)$, (ii) biaxial yield stress Y_b^{CP} on the yield surface in RD-TD, RD-ND and TD-ND planes. Then the well-known non-linear least-square method Levenberg—Marquardt algorithm was applied to determine the anisotropic coefficients of the yield function curve so that the sum of the squares of the deviations is minimized:

$$R(\alpha_i) = \frac{1}{n_1 + n_2 + n_3} \left\{ \sum_{i=1}^{n_1} \left(\frac{Y_u^{CP}(\theta)}{Y_u^{fun}(\theta)} - 1 \right)^2 + \sum_{i=1}^{n_2} \left(\frac{r_u^{CP}(\theta)}{r_u^{fun}(\theta)} - 1 \right)^2 \right.$$
$$\left. + \sum_{i=1}^{n_3} \left(\frac{Y_b^{CP}}{Y_b^{fun}} - 1 \right)^2 \right\} \Rightarrow \text{Min} \quad (40)$$

where superscript fun denotes the corresponding plastic anisotropy data calculated by yield function.

References

[1] Habraken AM, Aksen TA, Alves JL, Amaral RL, Betaieb E, Chandola N, et al. Analysis of ESAFORM 2021 cup drawing benchmark of an Al alloy, critical factors for accuracy and efficiency of FE simulations. Int J Mater Form 2022;15:61.

[2] Welo T, Ringen G, Ma J. An overview and evaluation of alternative forming processes for complex aluminium products. Procedia Manuf 2020;48:82–9.

[3] Liu W, Pang Y. A multi-scale modelling framework for anisotropy prediction in aluminium alloy sheet and its application in the optimisation of the deep-drawing process. Int J Adv Manuf Technol 2021;114(11):3401–17.

[4] Yang H, Li H, Ma J, Zhang Z, Chen J. Constitutive modeling related uncertainties: Effects on deformation prediction accuracy of sheet metallic materials. Int J Mech Sci 2019;157–158:574–98.

[5] Li H, Liu HR, Liu N, Sun H, Yang H, Liu BY. Towards sensitive prediction of wrinkling instability in sheet metal forming by introducing evolution of triple nonlinearity: Tube forming. Int J Mech Sci 2019;161–162:105054.

[6] Basak S, Panda SK, Lee M-G. Formability and fracture in deep drawing sheet metals: Extended studies for pre-strained anisotropic thin sheets. Int J Mech Sci 2020;170:105346.

[7] Sanchez L. Modeling of springback, strain rate and Bauschinger effects for two-dimensional steady state cyclic flow of sheet metal subjected to bending under tension. Int J Mech Sci 2010;52(3):429–39.

[8] Vega LRS, Hanzon DW. Quantification of large uniaxial Bauschinger effects in sheet metal from pure bending/unbending tests and interferometer techniques. Int J Mech Sci 2016;118:144–54.

[9] Kuwabara T, Sugawara F. Multiaxial tube expansion test method for measurement of sheet metal deformation behavior under biaxial tension for a large strain range. Int J Plast 2013;45:103–18.

[10] Kuwabara T, Mori T, Asano M, Hakoyama T, Barlat F. Material modeling of 6016-o and 6016-T4 aluminum alloy sheets and application to hole expansion forming simulation. Int J Plast 2017;93:164–86.

[11] Dick RE, Yoon JW. Plastic anisotropy and failure in thin metal: Material characterization and fracture prediction with an advanced constitutive model and polar EPS (effective plastic strain) fracture diagram for AA 3014-H19. Int J Solids Struct 2018;151:195–213.

[12] Hou Y, Min J, Guo N, Lin J, Carsley JE, Stoughton TB, et al. Investigation of evolving yield surfaces of dual-phase steels. J Mater Process Technol 2019;116314.

[13] Ma J, Yang H, Li H, Tao ZJ, Li GJ. Springback prediction of titanium tube bending considering Bauschinger effect and Young's modulus variation. J Phys Conf Ser 2016;734:032113.

[14] Min J, Guo N, Hou Y, Jiang K, Chen X, Carsley JE, et al. Effect of tension-compression testing strategy on kinematic model calibration and spring back simulation of advanced high strength steels. Int J Mater Form 2021;14(3):435–48.

[15] Barlat F, Aretz H, Yoon JW, Karabin ME, Brem JC, Dick RE. Linear transfomation-based anisotropic yield functions. Int J Plast 2005;21(5):1009–39.

[16] Yoon JW, Barlat F, Dick RE, Karabin ME. Prediction of six or eight ears in a drawn cup based on a new anisotropic yield function. Int J Plast 2006;22(1):174–93.

[17] Aretz H, Barlat F. New convex yield functions for orthotropic metal plasticity. Int J Non-Linear Mech 2013;51:97–111.

[18] Banabic D, Kuwabara T, Balan T, Comsa D, Julean D. Non-quadratic yield criterion for orthotropic sheet metals under plane-stress conditions. Int J Mech Sci 2003;45(5):797–811.

[19] Hershey A. The plasticity of an isotropic aggregate of anisotropic face-centered cubic crystals. 1954.

[20] Banabic D, Aretz H, Comsa D, Paraianu L. An improved analytical description of orthotropy in metallic sheets. Int J Plast 2005;21(3):493–512.

[21] Vrh M, Halilovič M, Starman B, Štok B, Comsa D-S, Banabic D. Capability of the BBC2008 yield criterion in predicting the earing profile in cup deep drawing simulations. Eur J Mech A Solids 2014;45:59–74.

[22] Raemy C, Manopulo N, Hora P. On the modelling of plastic anisotropy, asymmetry and directional hardening of commercially pure titanium: A planar Fourier series based approach. Int J Plast 2017;91:182–204.

[23] Hu Q, Yoon JW, Stoughton TB. Analytical determination of anisotropic parameters for Poly6 yield function. Int J Mech Sci 2021;201:106467.

[24] Safaei M, Lee M-G, Zang S-l, De Waele W. An evolutionary anisotropic model for sheet metals based on non-associated flow rule approach. Comput Mater Sci 2014;81:15–29.

[25] Yoshida F, Hamasaki H, Uemori T. Modeling of anisotropic hardening of sheet metals including description of the Bauschinger effect. Int J Plast 2015;75:170–88.

[26] Taylor GI. Plastic strain in metals. J Inst Metals 1938;62:307–24.

[27] Bishop J, Hill R. A theory of the plastic distortion of a polycrystalline aggregate. Phil. 1951.

[28] Kroner E. On the plastic deformation of polycrystals. Acta Metall 1961;9(2):155–61.

[29] Kocks UF. Polyslip in polycrystals. Acta Metall 1958;6(2):85–94.

[30] Hill R. Continuum micro-mechanics of elastoplastic polycrystals. J Mech Phys Solids 1965;13(2):89–101.

[31] Hutchinson JW. Bounds and self-consistent estimates for creep of polycrystalline materials. Proc R Soc Lond Ser A Math Phys Eng Sci 1976;348(1652):101–27.

[32] Lebensohn R, Tomé C. A study of the stress state associated with twin nucleation and propagation in anisotropic materials. Phil Mag A 1993;67(1):187–206.

[33] Lebensohn R, Tomé C. A self-consistent viscoplastic model: Prediction of rolling textures of anisotropic polycrystals. Mater Sci Eng A 1994;175(1–2):71–82.

[34] Lebensohn RA, Kanjarla AK, Eisenlohr P. An elasto-viscoplastic formulation based on fast Fourier transforms for the prediction of micromechanical fields in polycrystalline materials. Int J Plast 2012;32:59–69.

[35] Roters F, Eisenlohr P, Hantcherli L, Tjahjanto DD, Bieler TR, Raabe D. Overview of constitutive laws, kinematics, homogenization and multiscale methods in crystal plasticity finite-element modeling: Theory, experiments, applications. Acta Mater 2010;58(4):1152–211.

[36] Bong HJ, Lee J. Crystal plasticity finite element–Marciniak-Kuczynski approach with surface roughening effect in predicting formability of ultra-thin ferritic stainless steel sheets. Int J Mech Sci 2021;191:106066.

[37] Shi S, Li Y, Yan Z, Yang S, Ju Y. Crystal plasticity phase-field simulation of slip system anisotropy during creep of Co-Al-V monocrystal alloy under multidirectional strain. Int J Mech Sci 2022;227:107436.

[38] Bong HJ, Hu X, Sun X, Ren Y. Mechanism-based constitutive modeling of ZEK100 magnesium alloy with crystal plasticity and in-situ HEXRD experiment. Int J Plast 2019;113:35–51.

[39] Zhang K, Holmedal B, Hopperstad OS, Dumoulin S, Gawad J, Van Bael A, et al. Multi-level modelling of mechanical anisotropy of commercial pure aluminium plate: Crystal plasticity models, advanced yield functions and parameter identification. Int J Plast 2015;66:3–30.

[40] Zhang H, Diehl M, Roters F, Raabe D. A virtual laboratory using high resolution crystal plasticity simulations to determine the initial yield surface for sheet metal forming operations. Int J Plast 2016;80:111–38.

[41] Liu W, Chen B, Pang Y. Numerical investigation of evolution of earing, anisotropic yield and plastic potentials in cold rolled FCC aluminium alloy based on the crystallographic texture measurements. Eur J Mech, A/Solids 2019;75.

[42] Roters F, Diehl M, Shanthraj P, Eisenlohr P, Reuber C, Wong SL, et al. DAMASK– the Düsseldorf advanced material simulation kit for modeling multi-physics crystal plasticity, thermal, and damage phenomena from the single crystal up to the component scale. Comput Mater Sci 2019;158:420–78.

[43] Gui Y, An D, Han F, Lu X, Kang G, Zhang X. Multiple-mechanism and microstructure-based crystal plasticity modeling for cyclic shear deformation of TRIP steel. Int J Mech Sci 2022;222:107269.

[44] Liu W, Chen BK, Pang Y, Najafzadeh A. A 3D phenomenological yield function with both in and out-of-plane mechanical anisotropy using full-field crystal plasticity spectral method for modelling sheet metal forming of strong textured aluminum alloy. Int J Solids Struct 2020;193–194:117–33.

[45] Li Q, Zhang H, Chen F, Xu D, Sui D, Cui Z. Study on the plastic anisotropy of advanced high strength steel sheet: Experiments and microstructure-based crystal plasticity modeling. Int J Mech Sci 2020;176:105569.

[46] Isavand S, Assempour A. Strain localization and deformation behavior in ferrite-pearlite steel unraveled by high-resolution in-situ testing integrated with crystal plasticity simulations. Int J Mech Sci 2021;200:106441.

[47] Zheng JY, Ran J, Fu MW. Constitutive modeling of multiscale polycrystals considering grain structures and orientations. Int J Mech Sci 2022;216:106992.

[48] Feng Z, Li H, Zhang D, Guo X, Chen Y, Fu MW. Multi-aspect size effect transition from micro to macroscale: Modelling and experiment. Int J Plast 2022;156:103364.

[49] Eisenlohr P, Diehl M, Lebensohn RA, Roters F. A spectral method solution to crystal elasto-viscoplasticity at finite strains. Int J Plast 2013;46:37–53.

[50] Shanthraj P, Eisenlohr P, Diehl M, Roters F. Numerically robust spectral methods for crystal plasticity simulations of heterogeneous materials. Int J Plast 2015;66:31–45.

[51] Liu W, Huang J, Liu J, Wu X, Zhang K, Huang A. Experimental and crystal plasticity modelling study on the crack initiation in micro-texture regions of Ti-6Al-4V during high cycle fatigue tests. Int J Fatigue 2021;148:106203.

[52] Ferreri NC, Feng Z, Savage DJ, Brown DW, Clausen B, Sisneros TA, et al. In-situ high-energy X-ray diffraction and crystal plasticity modeling to predict the evolution of texture, twinning, lattice strains and strength during loading and reloading of beryllium. Int J Plast 2022;150:103217.

[53] Guo N, Wang J, Sun C, Zhang Y, Fu M. Analysis of size dependent earing evolution in micro deep drawing of TWIP steel by using crystal plasticity modeling. Int J Mech Sci 2020;165:105200.

[54] Yang H, Li H, Sun H, Zhang Y, Liu X, Zhan M, et al. Anisotropic plasticity and fracture of alpha titanium sheets from cryogenic to warm temperatures. Int J Plast 2022;156:103348.

[55] Ma H, Li Y, Zhang H, Li Q, Chen F, Cui Z. A virtual laboratory based on full-field crystal plasticity simulation to characterize the multiscale mechanical properties of AHSS. Sci Rep 2022;12(1):1–16.

[56] Mamun A, Moat R, Kelleher J, Bouchard P. Origin of the Bauschinger effect in a polycrystalline material. Mater Sci Eng A 2017;707:576–84.

[57] Bong HJ, Lim H, Lee M-G, Fullwood DT, Homer ER, Wagoner RH. An RVE procedure for micromechanical prediction of mechanical behavior of dual phase steel. Mater Sci Eng A 2017;695:101–11.

[58] Li YL, Kohar CP, Muhammad W, Inal K. Precipitation kinetics and crystal plasticity modeling of artificially aged AA6061. Int J Plast 2022;103241.

[59] Zhang X, Lu X, Zhao J, Kan Q, Li Z, Kang G. Temperature effect on tensile behavior of an interstitial high entropy alloy: Crystal plasticity modeling. Int J Plast 2022;150:103201.

[60] Yoshida F, Uemori T. A model of large-strain cyclic plasticity describing the Bauschinger effect and workhardening stagnation. Int J Plast 2002;18(5–6):661–86.

[61] Chung K, Lee M-G, Kim D, Kim C, Wenner ML, Barlat F. Spring-back evaluation of automotive sheets based on isotropic-kinematic hardening laws and non-quadratic anisotropic yield functions: Part I: Theory and formulation. Int J Plast 2005;21(5):861–82.

[62] Lee MG, Kim D, Kim C, Wenner M, Wagoner R, Chung K. A practical two-surface plasticity model and its application to spring-back prediction. Int J Plast 2007;23(7):1189–212.

[63] Ghaei A, Green D. Numerical implementation of Yoshida–Uemori two-surface plasticity model using a fully implicit integration scheme. Comput Mater Sci 2010;48(1):195–205.

[64] Yoshida F, Hamasaki H, Uemori T. Modeling of anisotropic hardening of sheet metals including description of the Bauschinger effect. Int J Plast 2015;75:170–88.

[65] Ghaei A, Taherizadeh A. A two-surface hardening plasticity model based on non-associated flow rule for anisotropic metals subjected to cyclic loading. Int J Mech Sci 2015;92:24–34.

[66] Barlat F, Gracio JJ, Lee M-G, Rauch EF, Vincze G. An alternative to kinematic hardening in classical plasticity. Int J Plast 2011;27(9):1309–27.

[67] Barlat F, Vincze G, Grácio J, Lee M-G, Rauch E, Tomé C. Enhancements of homogenous anisotropic hardening model and application to mild and dual-phase steels. Int J Plast 2014;58:201–18, In Honor of Kwansoo Chung.

[68] Kim JH, Kim D, Barlat F, Lee M-G. Crystal plasticity approach for predicting the Bauschinger effect in dual-phase steels. Mater Sci Eng A 2012;539:259–70.

[69] Li L, Shen L, Proust G. A texture-based representative volume element crystal plasticity model for predicting Bauschinger effect during cyclic loading. Mater Sci Eng A 2014;608:174–83.

[70] Li YL, Kohar CP, Mishra RK, Inal K. A new crystal plasticity constitutive model for simulating precipitation-hardenable aluminum alloys. Int J Plast 2020;132:102759.

[71] Gui Y, An D, Han F, Lu X, Kang G, Zhang X. Multiple-mechanism and microstructure-based crystal plasticity modeling for cyclic shear deformation of TRIP steel. Int J Mech Sci 2022;222:107269.

[72] Agaram S, Srinivasan SM, Kanjarla AK. Crystal plasticity modelling of stability of residual stresses induced by shot peening. Int J Mech Sci 2022;230:107526.

[73] le Graverend J-B. Crystal-plasticity modeling of monotonic and cyclic softening in inconel 718 superalloy. Int J Mech Sci 2023;239:107871.

[74] Hutchinson JW. Bounds and self-consistent estimates for creep of polycrystalline materials. Proc R Soc Lond Ser A Math Phys Eng Sci 1976;348(1652):101–27.

[75] Peirce D, Asaro RJ, Needleman A. Material rate dependence and localized deformation in crystalline solids. Acta Metall 1983;31(12):1951–76.

[76] Brown SB, Kim KH, Anand L. An internal variable constitutive model for hot working of metals. Int J Plast 1989;5(2):95–130.

[77] Barlat F, Brem JC, Yoon JW, Chung K, Dick RE, Lege DJ, et al. Plane stress yield function for aluminum alloy sheets - Part 1: Theory. Int J Plast 2003;19(9):1297–319.

[78] Yoshida F, Uemori T. A model of large-strain cyclic plasticity and its application to springback simulation. Int J Mech Sci 2003;45(10):1687–702.

[79] Quey R, Renversade L. Optimal polyhedral description of 3D polycrystals: Method and application to statistical and synchrotron X-ray diffraction data. Comput Methods Appl Mech Engrg 2018;330:308–33.

[80] Hielscher R, Schaeben H. A novel pole figure inversion method: Specification of the MTEX algorithm. J Appl Crystallogr 2008;41(6):1024–37.

[81] Fan Z, Lei X, Wang L, Yang X, Sanders RE. Influence of quenching rate and aging on bendability of AA6016 sheet. Mater Sci Eng A 2018;730:317–27.

[82] Zhao Z, Ramesh M, Raabe D, Cuitiño A, Radovitzky R. Investigation of three-dimensional aspects of grain-scale plastic surface deformation of an aluminum oligocrystal. Int J Plast 2008;24(12):2278–97.

[83] Tucker G. Texture and earing in deep drawing of aluminium. Acta Metall 1961;9(4):275–86.

[84] Darrieulat M, Piot D. A method of generating analytical yield surfaces of crystalline materials. Int J Plast 1996;12(5):575–610.